

# RELATIVISTIC ATOMIC STRUCTURE CALCULATIONS APPLIED TO ELECTRONIC TRANSITIONS IN ATOMS

ANNA SANKARI

*Department of Physical Sciences  
University of Oulu  
Finland*

Academic Dissertation to be presented with the assent of the Faculty of Science, University of Oulu, for public discussion in the Auditorium L10, on March 7th, 2008, at 12 o'clock noon.

**Opponent**

Prof. J. Tulkki, Helsinki University of Technology, Finland

**Reviewers**

Prof. J. Tulkki, Helsinki University of Technology, Finland

Prof. A.N. Grum-Grzhimailo, Moscow State University, Russia

**Custos**

Prof. H. Aksela, University of Oulu, Finland

ISBN 978-951-42-8727-5

ISSN 1239-4327

OULU UNIVERSITY PRESS

Oulu 2008

**Sankari, Anna: Relativistic atomic structure calculations applied to electronic transitions in atoms**

Department of Physical Sciences, University of Oulu, FINLAND  
Report No. 48 (2008)

## **Abstract**

In this thesis, the electronic structure of selected atoms was investigated by means of electron and fluorescence spectroscopy. Synchrotron radiation was used to excite atoms in gas phase. In particular, the photoionization and subsequent Auger decay processes in metal vapours were studied as well as the resonant Auger decay in rare gases. The experimental results were analyzed together with theoretical predictions obtained utilizing the multi-configuration Dirac-Fock method.

*Key words:* Electron spectroscopy, photoionization, Auger decay, synchrotron radiation, fluorescence spectroscopy.



# Acknowledgments

This work has been carried out at the Department of Physical Sciences at the University of Oulu. I would like to thank the Head of the Department, Prof. Jukka Jokisaari, as well as the personnel of the Department for placing the facilities at my disposal. I am very grateful to my supervisor Prof. Helena Aksela and Prof. Seppo Aksela for not only providing the essential tools required to perform the experiments and calculations in this work but also for sharing their invaluable knowledge and enthusiasm for atomic physics. Thank you for your guidance, support, and patience.

I also want to acknowledge docent Sami Heinäsmäki for his patient guidance. I am deeply indebted for the opportunity to work with docent Antti Kivimäki. His guidance and support is gratefully acknowledged. I am very thankful for all (especially senior and some former) members of the Electron Spectroscopy group who have helped me with the small but crucial steps of this work. Special thanks are dedicated to Leena with whom I have also shared the ups and downs related to this work.

In addition, Dr. Lorenzo Avaldi, Dr. Kevin Prince, and the other members of the Gas-Phase Beamline group are acknowledged for their hospitality during my visit at ELETTRA. I am also very grateful to Prof. Edwin Kukk and the group of Materials Science for hosting my stay for the past few years at the University of Turku. I would also like to thank the National Graduate School in Material Physics, the Vilho, Yrjö, and Kalle Väisälä Foundation, the Finnish Cultural Foundation, and the Faculty of Science at the University of Oulu for the funding I have received.

Last, but certainly not least, my deepest gratitude belongs to my dear family, relatives, and friends for being there for me. Especially, I would like to acknowledge Aili for her contribution as well as my godsons Kasper and Vincent who have brought so much joy to my life together with their families. This thesis (as well as many other things) would not have been possible without the enormous support I have received from my parents and siblings over the years. I am also very lucky for being able to share my life with a soul mate - thank you for finding me, Rami.

Oulu, February 2008      Anna Sankari

## LIST OF ORIGINAL PAPERS

The present thesis contains an introductory part and the following papers which will be referred to in the text by their Roman numbers.

- I. **A. Penttilä**, S. Heinäsmäki, M. Harkoma, S. Fritzsche, R. Sankari, S. Aksela, and H. Aksela, *Effects of electron correlation on the decay process following the 3p photoionization in atomic manganese*, Physical Review A **71**, 022715 (2005).
- II. **A. Sankari**, R. Sankari, S. Heinäsmäki, M. Huttula, S. Aksela, and H. Aksela, *4d photoionization and subsequent Auger decay in atomic Eu*, submitted to Physical Review A.
- III. **A. Sankari**, S. Alitalo, S. Fritzsche, J. Nikkinen, A. Kivimäki, S. Aksela, and H. Aksela, *Excitation-energy dependence of the resonant Auger transitions to the  $4p^4(^1D)np$  ( $n = 5, 6$ ) states across the  $3d_{3/2}^{-1}5p$  and  $3d_{5/2}^{-1}6p$  resonances in Kr*, Physical Review A **76**, 022702 (2007); Erratum, Physical Review A **76**, 069902(E) (2007).
- IV. **A. Sankari**, R. Sankari, S. Heinäsmäki, S. Aksela, H. Aksela, A. Kivimäki, M. Coreno, M. de Simone, and K.C. Prince, *Interference effects in the decay of the  $3d \rightarrow 5p, 6p$  excitations of Kr studied with fluorescence spectroscopy*, accepted for publication in Physical Review A.
- V. **A. Penttilä**, S. Heinäsmäki, R. Sankari, S. Aksela, and H. Aksela, *Resolution enhancement by deconvolution*, Journal of Electron Spectroscopy and Related Phenomena **144-147**, 979 (2005).

The author has participated in the measurements related to all papers except Paper III and the multiconfiguration Dirac-Fock calculations for all included papers excluding the direct photoionization amplitudes in Paper III computed by S. Fritzsche. The Hartree-Fock calculations in Paper IV were performed by R. Sankari. The author has also analyzed the experimental data for all papers except Paper III and been the corresponding author in all papers.

In addition, the author has participated in the following paper that is not included in this thesis.

1. E. Kukk, R. Sankari, M. Huttula, **A. Sankari**, H. Aksela, and S. Aksela, *New electron-ion coincidence setup at MAX-II: fragmentation of acetonitrile following N 1s core excitation*, Journal of Electron Spectroscopy and Related Phenomena **155**, 141 (2007).



# Contents

<b>Abstract</b>	<b>i</b>
<b>Acknowledgments</b>	<b>iii</b>
<b>List of original papers</b>	<b>iv</b>
<b>Contents</b>	<b>vii</b>
<b>1 Introduction</b>	<b>1</b>
<b>2 Electronic transitions</b>	<b>3</b>
2.1 Atomic state . . . . .	3
2.2 Photoabsorption . . . . .	5
2.3 Decay processes . . . . .	6
2.3.1 Radiative decay . . . . .	6
2.3.2 Non-radiative Auger decay . . . . .	7
2.4 Selection rules . . . . .	9
2.5 Angular distribution . . . . .	9
<b>3 Experiment</b>	<b>13</b>
3.1 Synchrotron radiation . . . . .	13
3.2 End stations . . . . .	15
3.2.1 Hemispherical electron analyzer . . . . .	16
3.2.2 Fluorescence spectrograph . . . . .	18
3.3 Line width . . . . .	19
<b>4 Data analysis</b>	<b>23</b>
4.1 Corrections . . . . .	23
4.1.1 Energy calibration . . . . .	23
4.1.2 Transmission correction . . . . .	24
4.1.3 Detector efficiency . . . . .	24
4.1.4 Variations in experimental conditions . . . . .	25
4.2 Data processing . . . . .	25
4.3 Deconvolution . . . . .	26

<b>5</b>	<b>Calculations</b>	<b>27</b>
5.1	Wave functions and energies . . . . .	27
5.2	Transition probabilities . . . . .	29
5.2.1	Photon-atom interaction . . . . .	29
5.2.2	Coulomb interaction . . . . .	30
5.2.3	Resonant photoionization . . . . .	32
<b>6</b>	<b>Summary of the included papers</b>	<b>35</b>
	<b>Bibliography</b>	<b>43</b>

## ORIGINAL PAPERS

# Chapter 1

## Introduction

The fundamental purpose of physics is to understand and explain the observed physical phenomena. Theories, laws, and principles have been formulated to describe the behaviour of matter and its interactions. Even more important than seeking regularities in observations is questioning the current beliefs and suggesting alternative explanations. After centuries of critical examinations of physical theories we can no longer expect such a revolutionary new idea as the concept of light quanta introduced by Planck in 1901 [1] that began the era of modern physics and led to the development of quantum mechanics.

The foundations of quantum mechanics such as the Schrödinger wave equation [2] and Heisenberg uncertainty principle [3] were discovered as early as in the 1920's. Exact solution of the Schrödinger equation for a many-electron system cannot be found and therefore many approximative numerical methods have been derived decades ago (e.g. [4]). However, these numerical methods require huge computational resources and progress in computing power has enabled the application of the theoretical methods in practice bit by bit.

The quality of theoretical predictions is always tested by comparing the results with experimental data. The devices that are used to obtain experimental results, such as the synchrotron radiation light sources used in this work, are constantly under development and new, more precise measurements are performed all the time which leads to a demand for more precise theoretical predictions and new kinds of calculations.

In the present thesis, the experimental results obtained with electron and fluorescence spectroscopy are compared with calculated predictions. The calculations have been performed using pre-existing programs in order to test their applicability and the quality of the obtained results. In Papers I-II, the photoelectron and normal Auger spectra of metal atoms (Mn and Eu) have been measured with high resolution and the results have been compared with the calculations. In Papers III-V, the resonant Auger decay of Kr and

Ne has been investigated again together with the calculations. Before the discussion of the included papers, the used concepts and both experimental and theoretical methods are briefly introduced.

# Chapter 2

## Electronic transitions

The discovery of the electron in 1897 [5] revealed that atoms have an internal structure. Until then, atoms had been considered to be the smallest building blocks of all matter. In fact, atoms are composed of a very small, heavy, and positively-charged nucleus (containing protons and neutrons) surrounded by a negatively-charged electron cloud. It is the electron cloud that dictates most of the physical and chemical properties of the atom such as its reactivity, electronegativity, the way it forms compounds and so forth. Therefore, understanding the structure and dynamics of the electron cloud is of fundamental importance and the motivation of this thesis.

### 2.1 Atomic state

Electrons do not revolve arbitrarily around the nucleus but are confined to certain regions in space. Within the central-field approximation, the electron states are specified by three quantum numbers  $n$ ,  $l$ , and  $m_l$  as depicted in Fig. 2.1. In addition a fourth quantum number ( $m_s$ ) is needed to determine the state of an atomic electron explicitly. The principal quantum number  $n$  ( $n = 0, 1, 2, \dots$ ) defines a shell and the orbital angular momentum quantum number  $l$  ( $l = 0, 1, \dots, n - 1$ ) divides the shell into subshells. Instead of the orbital magnetic quantum number  $m_l$  ( $m_l = -l, \dots, l - 1, l$ ) and the spin magnetic quantum number  $m_s$  ( $m_s = \pm 1/2$ ), the total angular momentum quantum number  $j$  ( $j = l \pm 1/2$ ) and its magnetic quantum number  $m_j$  ( $m_j = -j, \dots, j - 1, j$ ) is also used, in particular for heavy elements and more generally for atomic inner shells.

In the ground state of a many-electron atom, the subshells are filled in a way that minimizes the total energy of the atom starting from the smallest  $n$  and  $l$  values. Obeying the Pauli exclusion principle [7] according to which no two electrons can share the same set of quantum numbers, the occupation of a subshell  $nl$  is limited to the number equal to  $2(2l + 1)$ . The occupation of the subshells in an atom is often given in the form  $(n_1l_1)^{q_1}(n_2l_2)^{q_2} \dots (n_kl_k)^{q_k}$

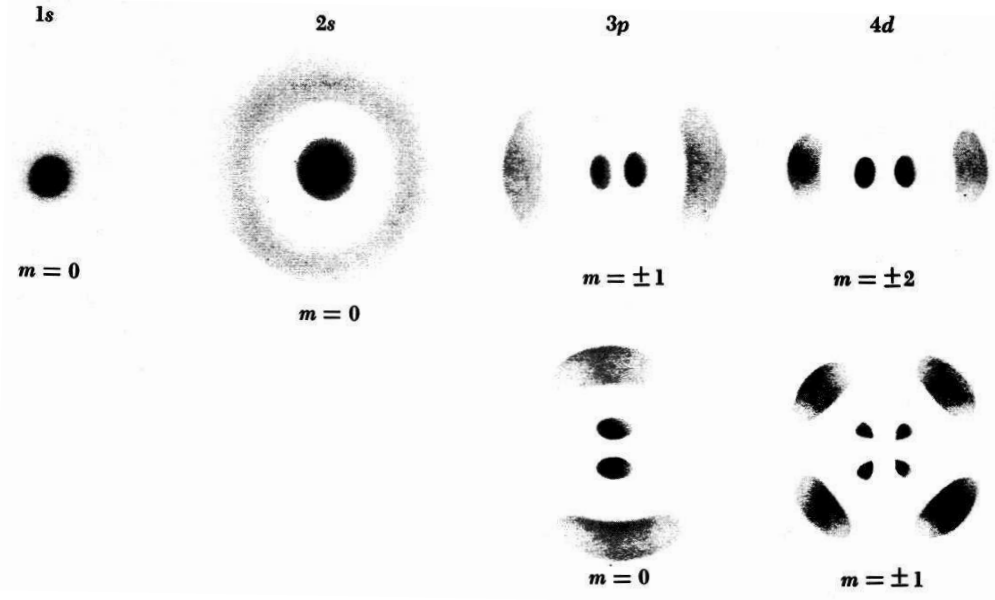


Figure 2.1: Atomic orbitals ( $nl$ ) for different combinations of  $n$ ,  $l$ , and  $m_l$  (modified from [6]).

(where  $l$  is denoted as  $s, p, d, f, \dots$  corresponding to values  $0, 1, 2, 3, \dots$  and  $q_k$  gives the occupation of the subshell  $k$ ) which is referred to as electron configuration. For the ground state of Ne, the electron configuration is  $1s^2 2s^2 2p^6$  and all the shells are said to be filled. In Mn ( $[\text{Ar}]3d^5 4s^2$ ) and Eu ( $[\text{Xe}]4f^7 6s^2$ ),  $3d$  and  $4f$  shells, respectively, are half-filled while all the other shells are filled in the ground state.

The orbital angular momentum,  $\mathbf{l}$ , and the spin angular momentum,  $\mathbf{s}$ , of an electron in a many-electron atom are coupled together as well as with the momenta of the other electrons in order to form the total angular momentum,  $\mathbf{J}$ , of the atom. In the  $LS$ -coupling scheme, the orbital and spin angular momenta of electrons are coupled first separately

$$\mathbf{L} = \sum_i \mathbf{l}_i \quad \mathbf{S} = \sum_i \mathbf{s}_i, \quad (2.1)$$

where  $\mathbf{L}$  and  $\mathbf{S}$  are the total orbital and spin angular momenta of the atom. These are then coupled together to give the total angular momentum

$$\mathbf{J} = \mathbf{L} + \mathbf{S}. \quad (2.2)$$

A particular atomic state described by the angular momenta  $L$ ,  $S$ , and  $J$  is often denoted by a shorthand notation

$$^{2S+1}L_J, \quad (2.3)$$

where numerical values are used for  $2S+1$  and  $J$ , and  $L$  is replaced by an appropriate capital letter ( $S, P, D, F, \dots$  corresponding to values  $0, 1, 2, 3, \dots$ ). [4]

Due to historical reasons, the  $LS$ -symbols are still used even though in relativistic calculations, such as those performed in all included papers, another coupling scheme is used. In the  $jj$ -coupling scheme, the total angular momentum of an electron is first obtained by coupling its  $\mathbf{l}$  and  $\mathbf{s}$

$$\mathbf{j} = \mathbf{l} + \mathbf{s}. \quad (2.4)$$

The total angular momenta of the electrons are then coupled together in order to determine the total angular momentum of the atom [8]

$$\mathbf{J} = \sum_i \mathbf{j}_i. \quad (2.5)$$

In case of completely filled subshells all of total angular momenta ( $L$ ,  $S$ , and  $J$ ) are zero (only possible state is thus  $^1S_0$ ) and therefore they are frequently omitted in notations. Often many electron states are a mixture of different  $LS$ -terms corresponding to the same total  $J$  value and naming the dominant term is a nontrivial issue.

## 2.2 Photoabsorption

The fundamental physical phenomenon, on which the photoelectron spectroscopy is based on, is the photoelectric effect first observed by Hertz in 1887 [9] and explained by Einstein in 1905 [10]. As an atom is irradiated with photons, a photon is absorbed and the energy of the photon ( $h\nu$ ) is transferred to an electron. If the energy exceeds the binding energy of the electron ( $E_B$ ), the electron is ejected from the atom with a kinetic energy ( $E_K$ ) equal to

$$E_K = h\nu - E_B. \quad (2.6)$$

In electron spectroscopy, the kinetic energies of the ejected electrons are analyzed which provides information about the photoionization process illustrated in Fig. 2.2(a). As a result, the atom  $X$  is ionized



and a vacancy is created in the electron cloud. In Papers I-II, the photoionization process of metal vapours has been investigated.

If the energy of the photon is not enough to ionize an electron but equals to the energy needed to excite the electron to a higher-lying, unoccupied

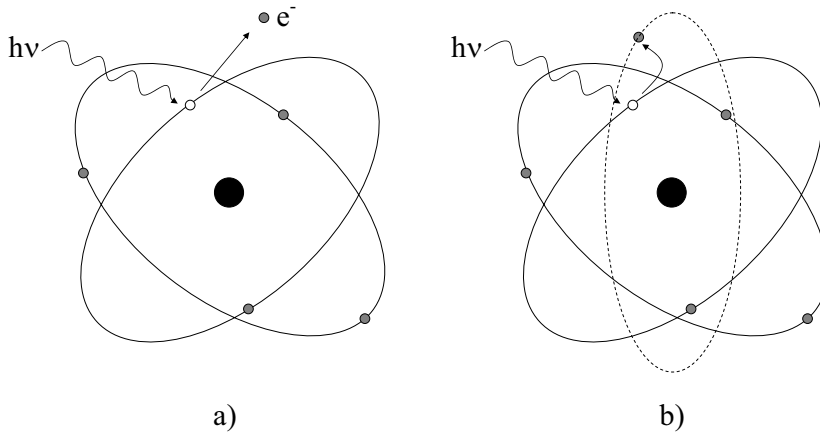


Figure 2.2: a) Photoionization and b) photoexcitation processes.

orbital  $nl$  (i.e.  $h\nu = E_{B,nl} - E_B$ ), a photoexcitation occurs [see Fig. 2.2(b)] and the atom is excited



Measuring the absorption spectrum by recording either the total ion or electron yield as a function of photon energy provides information about the structure of the electron cloud. In Fig. 2.3 the total ion yield spectrum of Kr recorded in the energy region of  $3d \rightarrow np$  ( $n \geq 5$ ) is shown. The spectrum is closely related to Papers III-IV where excitations to  $5p$  and  $6p$  orbitals were studied.

## 2.3 Decay processes

Absorption of a photon creates a vacancy in a subshell and the atom (or the created ion) is usually left in an excited state. According to the principle of minimum energy, the atom (or ion) will decay further until no vacancies can be found in the inner subshells. There are two kinds of decay processes which are often classified as radiative and non-radiative processes [12].

### 2.3.1 Radiative decay

The most familiar form of radiative decay processes is the visible UV-fluorescence radiation seen e.g. in auroras. It is a consequence of an electronic transition between the outer subshells e.g.  $3s \rightarrow 2p$  in Ne as shown in Fig. 2.4(a). The energy of the emitted photon is equal to the energy difference of the subshells, i.e. in this case

$$h\nu = E_{3s} - E_{2p}. \quad (2.9)$$

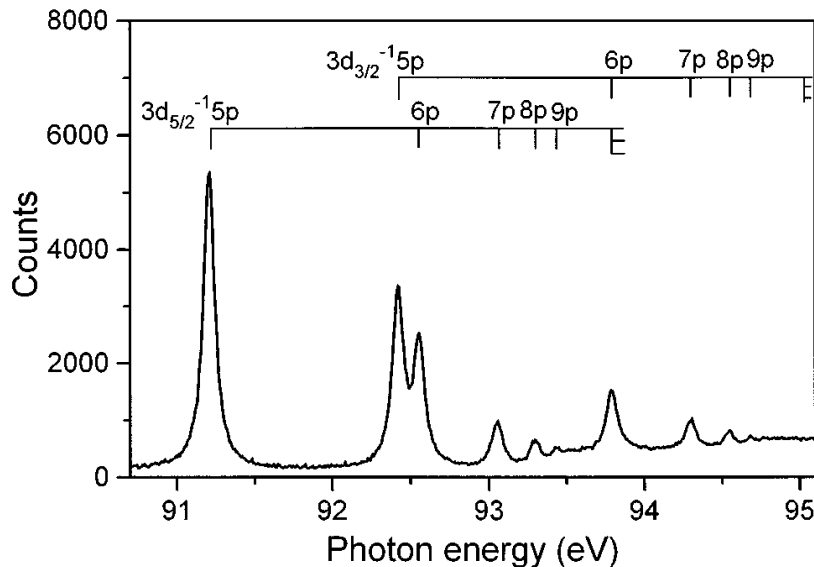


Figure 2.3: Total ion yield across the Kr  $3d \rightarrow np$  resonances [11].

In Paper IV, the visible fluorescence emitted in the transition  $4p^45p \rightarrow 4p^45s$  was investigated in Kr. If the initial vacancy is in the inner subshell, the same process is called X-ray fluorescence according to the energy of emitted photons [13].

Before electron spectroscopy, the electronic structure of atoms was investigated by means of optical spectroscopy. However, the fluorescence transitions obtained from excited atoms limit the investigation to valence shells and electron spectroscopy has substantially enlarged the data base of energy levels. Nevertheless, the optical data tables [14] are still widely used and they have served as useful references throughout this work.

### 2.3.2 Non-radiative Auger decay

In 1923, secondary electrons were observed after photoionization [15]. In Auger decay, the created vacancy is filled by an electron from an upper subshell and instead of a photon, one of the outer electrons is emitted [see Fig. 2.4(b)]. The kinetic energy of this Auger electron ( $E_K$ ) is obtained as the difference of the many-electron hole states as

$$E_K = E(\text{one-hole state}) - E(\text{two-hole state}) \quad (2.10)$$

and it depends only on the energy levels of the atom and not on the exciting photon energy. As the binding energies of photoelectrons and the wavelengths of emitted fluorescence, also the kinetic energies of Auger electrons are characteristic properties of atoms. Therefore, they are widely used e.g. in chemical analysis [16].

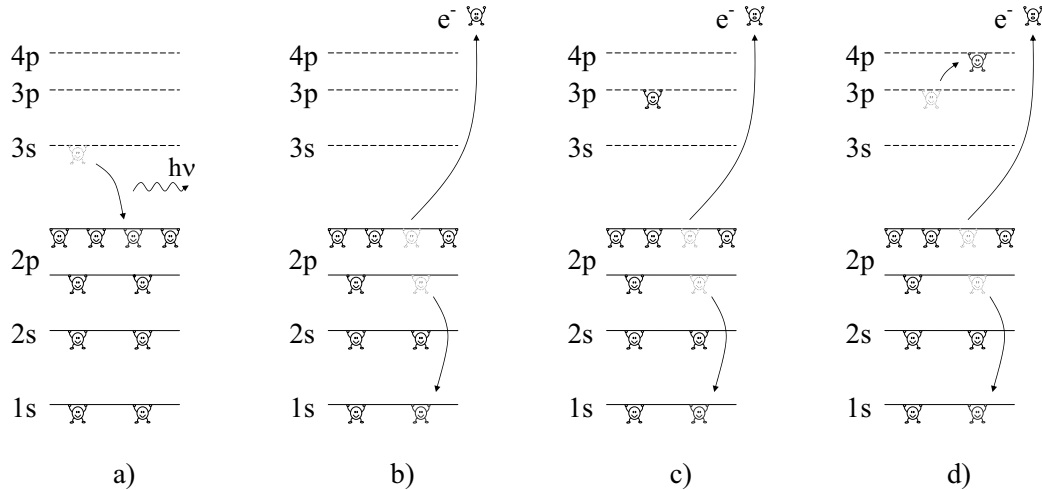


Figure 2.4: a) UV fluorescence emission due to the transition  $3s \rightarrow 2p$ , b) normal Auger decay ( $1s^{-1} \rightarrow 2p^{-2}$ ), c) spectator Auger decay ( $1s^{-1}3p \rightarrow 2p^{-2}3p$ ), and d) shake-up in the course of transition  $1s^{-1}3p \rightarrow 2p^{-2}4p$ .

The Auger transition following a photoionization [depicted in Fig. 2.4(b)] is called a normal Auger decay. If the vacancy and the other electron involved in the Auger decay are in the same shell, the process is called Coster-Kronig decay. If all three involved electrons are from the same shell, as in the  $3p^{-1} \rightarrow 3d^{-2}$  transition in Mn studied in Paper I, the process is called super-Coster-Kronig decay [17].

Three decades ago, in 1978, when synchrotron radiation provided the possibility to tune photon energy, Eberhardt *et al.* [18] observed resonant Auger lines for the first time. Resonant Auger decay follows a photoexcitation and if the excited electron does not participate in the Auger decay that fills the inner-shell vacancy, the process is known as spectator Auger decay [see Fig. 2.4(c)]. If the excited electron is ejected during the decay, the process is called participator Auger decay or autoionization [19].

During the spectator Auger decay, the excited electron can also 'shake up' (or down) to a higher (lower) unfilled orbital, which is illustrated in Fig. 2.4(d). In Papers III-IV, the resonant Auger decay of Kr has been studied by scanning the photon energy across the  $3d \rightarrow 5p$ ,  $6p$  resonances where the shake-up transitions have been shown to have remarkable contributions [20]. The resonant Auger spectrum following the  $1s \rightarrow 3p$  excitation in Ne, which was under investigation in Paper V, also has a clear shake-up contribution.

## 2.4 Selection rules

The above discussion introduced the electronic transitions that have been studied in the included papers. However, there are not just a multitude of transitions that can occur in an atom. Some transitions are stronger than others and some are hardly detectable. In a transition, the energy, angular momenta, and parity [defined as  $\Pi = (-1)^{\sum_i l_i}$ ] of the system are conserved. If one of the conservation laws is violated, the transition is forbidden i.e. it is most improbable.

In a dipole transition, which applies to photoexcitation and fluorescence emission, the initial and final states must have opposite parity ( $\Delta l = \pm 1$ ) and the angular momenta have to obey the following selection rules

$$\begin{aligned}\Delta L &= 0, \pm 1 \quad (\text{but not from } 0 \text{ to } 0), \\ \Delta S &= 0, \text{ and} \\ \Delta J &= 0, \pm 1 \quad (\text{but not from } 0 \text{ to } 0).\end{aligned}\tag{2.11}$$

In photoionization, the ejected electron (also referred to as a continuum electron) is coupled together with the final ionic state and together they satisfy the above conditions. [4]

Auger transitions are caused by the Coulomb interaction<sup>1</sup> between those electrons that participate directly in the transition [21]. Thus in Auger decay, the final state of the system, composed of the ion and the Auger electron, has to satisfy the selection rules

$$\Delta L = \Delta S = \Delta J = 0, \quad \Pi_i = \Pi_f.\tag{2.12}$$

A shake-up excitation is a result of a sudden, instantaneous change in the central potential of an atom which might occur e.g. in the course of Auger decay. The electron is initially on a  $nl$  orbital and after the change finds itself on another orbital ( $n'l$ ) as the orbitals are readjusted to the new potential. Shake-up is an example of a monopole transition, where only the principal quantum number ( $n$ ) changes [16].

## 2.5 Angular distribution

The experiments performed in all included papers have utilized linearly polarized synchrotron radiation and the following discussion is valid in case of linearly polarized light only. The polarization vector of the radiation serves as a reference plane and as a consequence of a photoionization (or excitation) the ion (atom) will be aligned [22]. The angular momentum of the photon

---

<sup>1</sup>The Coulomb interaction is mediated by a scalar operator and thus the angular momentum quantum numbers are preserved in an Auger transition.

is transferred to the electron and during the decay, it is shared between the outgoing electron and the ion [23]. This leads to nonisotropic angular distribution of the photoelectrons [24] as well as Auger electrons [25]. In dipole approximation<sup>2</sup>, the angular distribution of the electrons obeys the following relation

$$I_{\theta} = \frac{I_{\text{tot}}}{4\pi} [1 + \beta P_2(\cos \theta)], \quad (2.13)$$

where  $I_{\theta}$  is the intensity at an angle  $\theta$  with respect to the polarization vector,  $I_{\text{tot}}$  is the total intensity,  $\beta$  is the angular distribution parameter, and  $P_2(x)$  is the second order Legendre polynomial [ $P_2(x) = \frac{1}{2}(3x^2 - 1)$ ].

The  $\beta$  parameter can vary between -1 and +2 and the angular distribution of different  $\beta$  values are demonstrated in Fig. 2.5. Photoionization of  $ns$  electrons (in closed-shell atoms) leads to an angular distribution of  $\beta = 2$  [24]. However, some electrons are still emitted to the direction  $\theta = 90^\circ$  and deviations from  $\beta = 2$  are seen e.g. in the  $\beta$  value of Xe 5s in the threshold region [26].

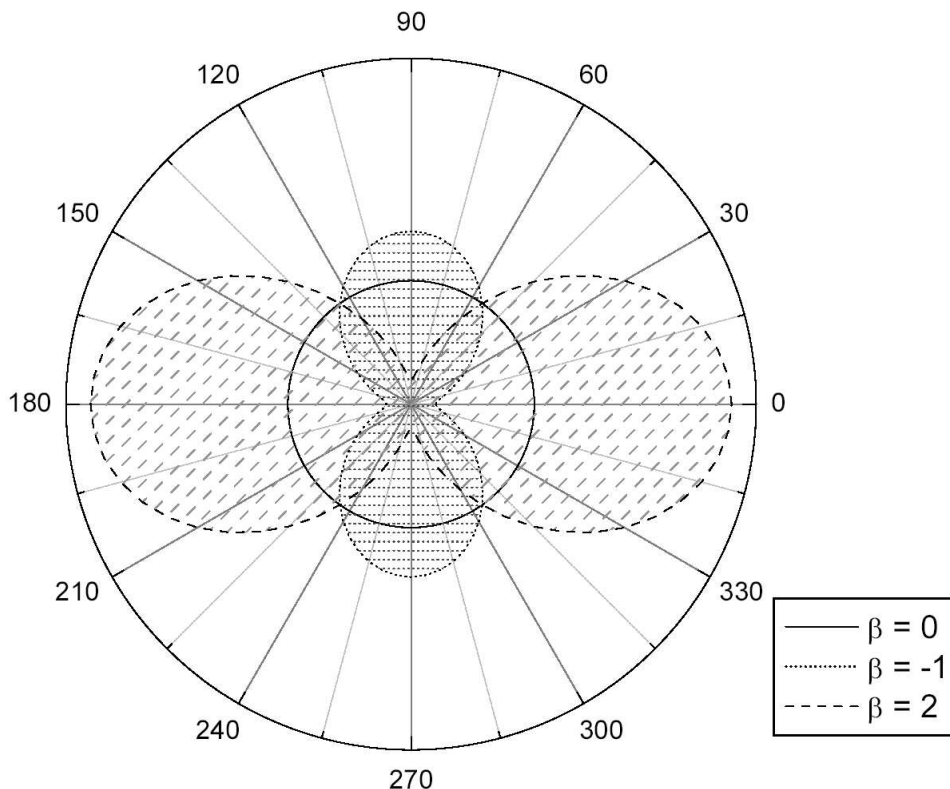


Figure 2.5: Angular distribution with  $\beta$  values -1, 0, and 2.

In Auger decay, the alignment of the initial state is shared between the

<sup>2</sup>Dipole approximation will be discussed in Chapt. 5.

ion and the Auger electron. The angular distribution parameter of the Auger electron depends on the polarization state in the initial state ( $\mathcal{A}_{20}$ ) and on a coefficient determined by the Auger decay amplitudes ( $\alpha_2$ ). In brief,  $\beta = \alpha_2 \mathcal{A}_{20}$  [25]. In Papers III and V, the  $\beta$  parameters of resonant Auger lines were determined from experimental spectra and compared with the calculated values.

The emitted fluorescence has also an angular distribution which obeys an equation similar to Eq. (2.13) if the fluorescence is detected regardless of the polarization of the emitted light [27]. This was the case in the measurements related to Paper V but the experimental settings did not allow measurements at different angles. The information provided by the angular distribution of the emitted fluorescence can also be obtained by studying the polarization of the photons. This is widely used in the determination of the alignment of excited states [28] but also angle-dependent fluorescence measurements have been performed [29].



# Chapter 3

## Experiment

In all Papers I-V, the main role has been on the experimental results. The calculations have been performed in order to explain the observed features and to test the limitations of computations. Without experimental baseline nothing can be said about the quality of theoretical results. In this chapter, the most essential aspects of the experiments related to the present thesis are discussed.

### 3.1 Synchrotron radiation

The fundamental basis of synchrotron radiation lies in the theory of electromagnetism according to which an accelerating charge produces electromagnetic radiation. Synchrotron radiation is generated when small, charged particles (such as electrons or positrons) are forced to move along a curved trajectory at relativistic speeds. Storage rings are special devices where electrons circulate and produce radiation when accelerated transversely. The storage rings include straight sections and curved sections as schematized in Fig. 3.1. The curved sections are bending magnets that bend the trajectories of the electrons and produce radiation as a by-product. [30]

Third-generation synchrotron facilities, such as MAX-II in Lund and ELETTRA in Trieste, have many straight sections where specially optimized insertion devices containing periodic magnetic structures produce very bright radiation. Insertion devices are classified to wigglers and undulators depending on the amplitude of the oscillations the electrons experience as they traverse the periodic magnetic field [see Fig. 3.2(a)] [31]. If the number of the magnetic periods is  $N$ , the flux produced in a wiggler is  $2N$  times that of a bending magnet, whereas the flux from an undulator is  $N^2$  times brighter [32].

The radiation emitted by electrons moving at relativistic speeds is concentrated around a direction tangential to the electron trajectory. In an undulator, relativistic effects lead to interference and a typical undulator

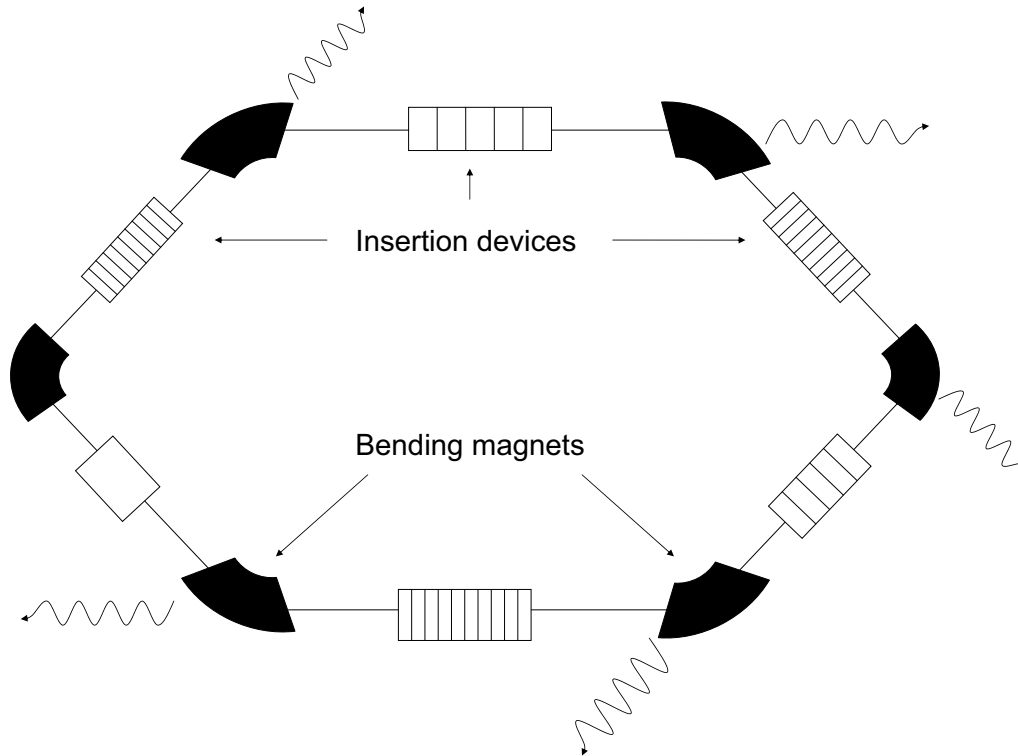


Figure 3.1: Illustration of a storage ring used to produce synchrotron radiation.

spectrum consists of several sharp peaks as shown in Fig. 3.2(b). In addition to a highly collimated photon beam and high intensity, synchrotron radiation is also highly polarized in the plane of the storage ring. This feature has been utilized in the angle-dependent measurements in Papers III and V. Without synchrotron radiation and the possibility to select any desired photon energy the resonant Auger decay studies (such as those in Papers III-V) would not have been feasible. Invaluable is also the high photon flux of third generation synchrotron radiation sources which is needed in the measurement of high-resolution electron spectra of metal vapours (Papers I-II) where a photon flux of at least  $10^{10} \frac{\text{photons}}{\text{s}}$  is required in the interaction region [34].

Before entering the experimental chamber, the radiation produced in the storage ring travels through a beamline. The optical elements (gratings, mirrors, and slits) of the beamline diffract, reflect, and spatially select the radiation. Due to optical properties of soft X-rays and vacuum ultra-violet radiation ( $h\nu > 50 \text{ eV}$ ) grazing incidence monochromators have to be used. Essentially all materials (including air) interact with the photons of these energies and therefore ultra high vacuum (UHV) is needed inside the beamlines. Typically, the pressure inside a monochromator chamber is  $10^{-10} \text{ mbar}$ . [32]

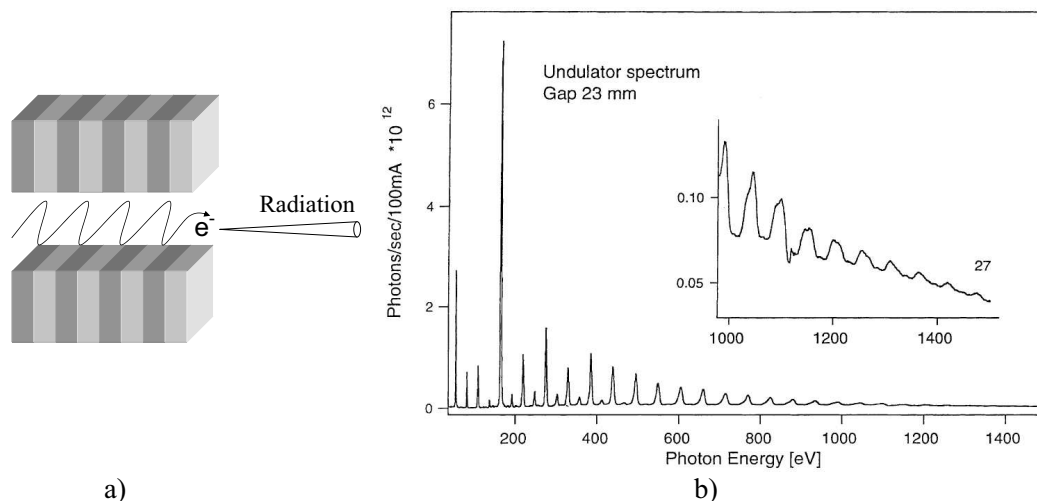


Figure 3.2: a) Path of the electrons in an undulator and b) the undulator spectrum at the beamline I411 [33].

Experiments in Papers I-III, and V have been performed at the beamline I411 (MAX-II) [33, 35] and the experimental part of Paper IV took place at the Gas-Phase Beamline (ELETTRA) [36]. Both of these beamlines are specially designed for gas phase measurements where the pressure in the experimental chamber is in the range of  $10^{-5}$ - $10^{-6}$  mbar. To avoid undesired pressure increase along the beamline, an additional differential pumping stage is necessary [33].

## 3.2 End stations

The discussion above is only concerned with the production of photons needed in the experiments. The actual measurements take place at the end stations of the beamlines. The spectrometer located at the end station is focused at the source volume (or interaction region) which is a small region ( $< 1 \text{ mm} \times 1 \text{ mm}$ ) where the photon beam intersects the target atoms in a gas cell or a gas jet produced by a gas needle or an oven. In the experiments of Papers I-II, a resistively heated oven (and also an induction oven) was used to produce an atom beam. In Papers III and V, a gas cell was used and in Paper IV, a gas needle produced the gas jet. In all experiments, the gas jet (if present), the photon beam and the focus of the spectrometer intersected perpendicularly to one another.

The measurement of electrons in Papers I-III, and V has been performed with a hemispherical electron analyzer, whereas a fluorescence spectrograph was used in Paper IV. These instruments are briefly described in the following.

### 3.2.1 Hemispherical electron analyzer

To analyze the kinetic energies of electrons, an electric or magnetic field is used in the energy dispersion. This is based on the Lorentz force according to which a charged particle (such as an electron) with a charge  $q$  moving with a velocity  $\mathbf{v}$  in an electric ( $\mathbf{E}$ ) and magnetic ( $\mathbf{B}$ ) field is subject to a force

$$\mathbf{F} = q(\mathbf{E} + \mathbf{v} \times \mathbf{B}). \quad (3.1)$$

The hemispherical analyzers SES-100 and SES-200 (manufactured by Scienta) use a constant electric field between two concentric hemispherical plates. The field is optimized so that only electrons with a specific energy can reach the detector on the opposite side of the hemisphere. This energy is called the pass energy of the spectrometer. The pass energy together with the entrance slit determine the energy resolution of the analyzer: in principle, the smaller the pass energy and/or the smaller the slit, the better the resolution.

However, a constant pass energy would be a major limitation of measurements if no electron with a kinetic energy other than the pass energy could be observed. For this reason, a retarding lens (a multi-element electrostatic lens) is mounted in front of the entrance slit of the analyzer. The selection of the kinetic energy of interest is made by decelerating (or accelerating) the electrons in the retarding lens before they traverse the entrance slit with the selected pass energy. [37]

Two kinds of experiments were performed in the present thesis. In Papers I-II, and V, the photon energy was kept constant and the kinetic energy of the electrons was scanned. In Paper III (as well as in Paper IV), a kinetic energy (or wavelength) region of interest was kept fixed and the photon energy was scanned. The latter type of experiment provides information about photon energy-dependent changes in the spectra.

The acceptance angle of a hemispherical analyzer is relatively small (less than  $\pm 10^\circ$ ). As a consequence, the transmission of the analyzer is also low, which is a disadvantage of these analyzers. On the other hand, the small acceptance angle offers also a possibility to perform angle-dependent measurements utilized in Papers III and V. As said before, the polarization vector of the incoming radiation together with the wave vector determine a reference plane which coincides with the plane of the storage ring. By rotating the analyzer with respect to this plane, measurements at different values of  $\theta$  in Eq. (2.13) can be carried out.

Convenient choices of the angle  $\theta$  are  $0^\circ$ ,  $54.7^\circ$ , and  $90^\circ$ , for which Eq. (2.13) reduces to

$$\begin{aligned} I_{0^\circ} &= \frac{I_{\text{tot}}}{4\pi}(1 + \beta) \\ I_{54.7^\circ} &= \frac{I_{\text{tot}}}{4\pi} \end{aligned} \quad (3.2)$$

$$I_{90^\circ} = \frac{I_{\text{tot}}}{4\pi} \left(1 - \frac{1}{2}\beta\right).$$

Measurement at two angles would be sufficient for the determination of the  $\beta$  parameter, but both in Papers III and V, the angle-dependent measurements were performed at three angles. Especially, if  $\beta = 2$  or  $\beta = -1$ , the use of two angles  $0^\circ$  and  $90^\circ$  in the determination of the  $\beta$  parameter leads to most uncertain results. For the experiments in Papers I-II, the analyzer was rotated to the so-called 'magic' angle ( $54.7^\circ$ ) to avoid any distortion of the intensities due to the angular dependence.

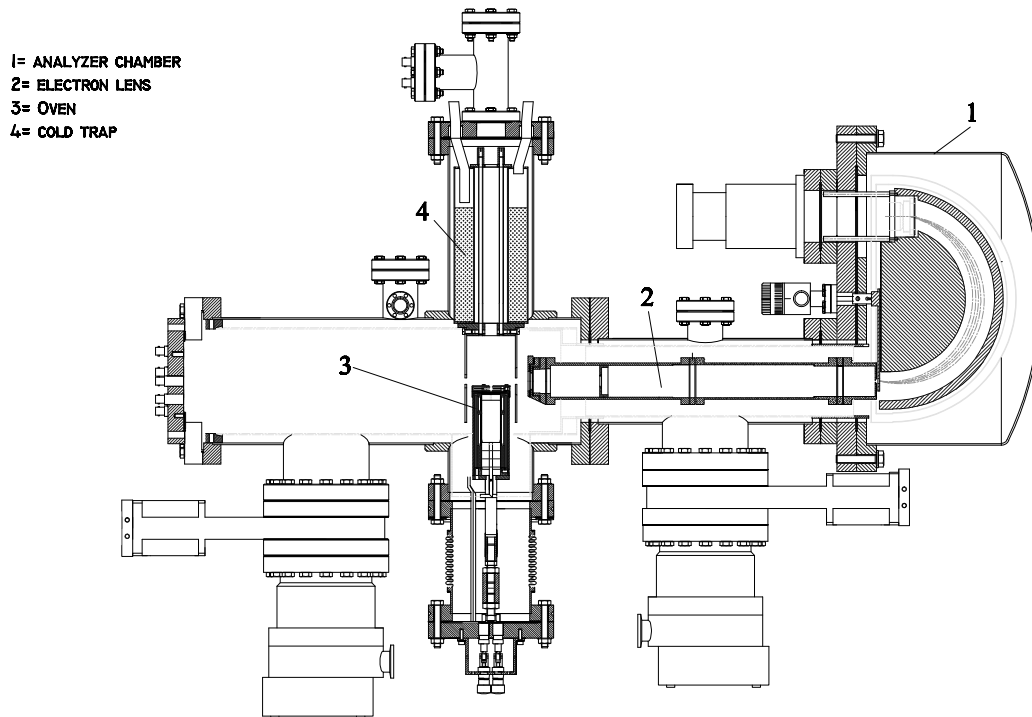


Figure 3.3: Hemispherical electron analyzer (1) mounted with a resistively heated oven (3) accompanied by a cold trap (4) perpendicular to the direction of the photon beam.

Figure 3.3 represents a schematic view of a hemispherical electron analyzer SES-100 used in the measurements of Papers I-II. The spectrometer was mounted on the one-meter section of the beamline I411 preceding the stationary end station, which comprises of a similar but bigger hemispherical analyzer (SES-200) [37]. The latter was used in the angle-dependent measurements of Papers III and V.

### 3.2.2 Fluorescence spectrograph

The apparatus used in the experimental part of Paper IV is schematized in Fig. 3.4. Unlike the electron analyzers, the UV-fluorescence spectrometers are operated in air, which limits the observed wavelength region above 200 nm. The experimental chamber was separated from the fluorescence monochromator by a quartz window. Opposite to the window a spherical mirror that reflected the emitted fluorescence towards the monochromator was mounted. After the quartz window, a lens focused the fluorescence into the entrance slit, which determines the resolution of the spectrograph (and restricts the transmission). A Czerny-Turner type monochromator (manufactured by McPherson) was used and a nitrogen-cooled charge-coupled device (CCD) camera (from Roper Scientific) registered the fluorescence spectra. The fluorescence monochromator was in the plane of the polarization vector of synchrotron radiation (i.e.  $\theta = 0$ ) and therefore the obtained results in Paper IV are angle-dependent.

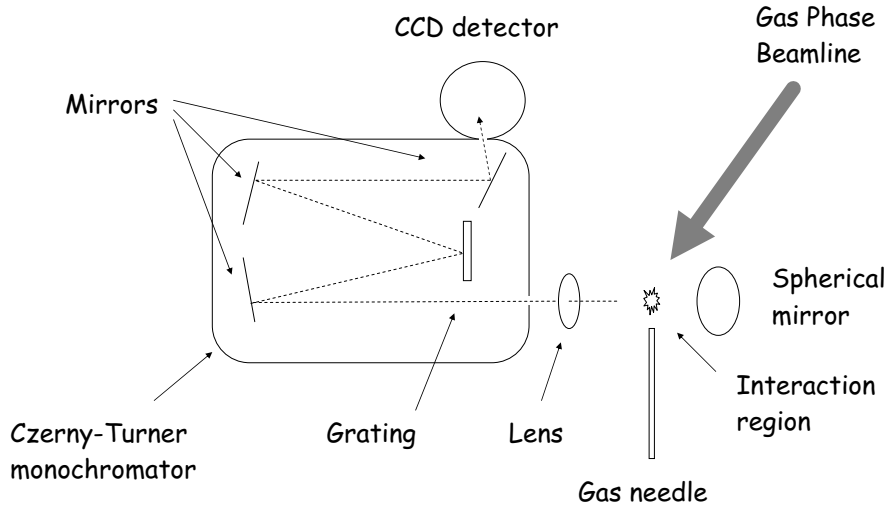


Figure 3.4: Schematic view of the fluorescence spectrograph used in Paper IV.

Fluorescence spectrometry has experienced a renaissance during the past two decades after it was first combined with the endless possibilities of synchrotron radiation. This photon-induced fluorescence spectroscopy (PIFS) offers a competent tool for investigating excited states that radiate [38, 39]. For instance, no other technique is capable of studying neutral but excited fragments that cannot decay via autoionization (such as  $H^*$ ) created in a molecular dissociation [40]. In addition to molecular dissociation investigations, many of the PIFS studies (see e.g. [41] for early works, and Paper IV or [42] for recent studies) have been dedicated to investigating photon energy dependence in rare gas atoms.

The inherently high resolution of fluorescence spectroscopy is the major advantage of the method in comparison with electron spectroscopy. The major drawback of PIFS is related to the cascade contribution [39, 43]. The intensity of the fluorescence depends only on the population of its initial state but it is insensitive to the different routes populating it. Thus, if the fluorescence originating from a resonant Auger final state (populated nonradiatively via direct photoionization or resonant Auger decay) is investigated, one has to remember that radiative processes (cascade transitions from higher-lying states) can also populate the same state. This complicates the study of a specific decay process preceding the fluorescence decay as noted in Paper IV.

### 3.3 Line width

A spectral line observed in a fluorescence or electron spectrum is not infinitely narrow but has a width that is a result of different line broadening mechanisms. The profile of the line depends on the profiles of the contributing broadening mechanisms. Usually, these are approximated by a Gaussian or a Lorentzian distribution which are depicted in Fig. 3.5. Figure 3.5 also shows a Voigt profile, which results from the convolution of a Lorentzian and a Gaussian profile. [12]

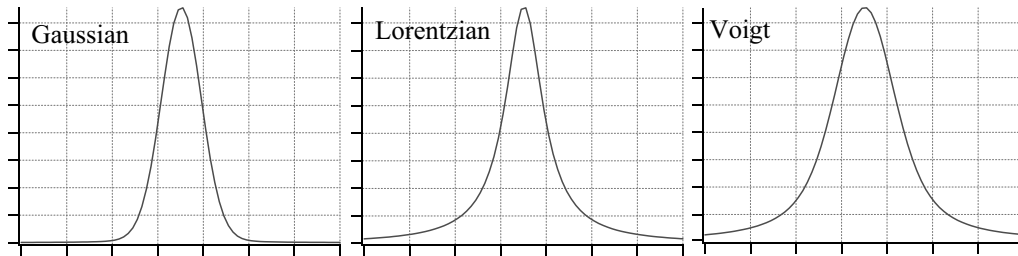


Figure 3.5: Gaussian, Lorentzian and Voigt profiles. Voigt profile has an equal contribution from Gaussian and Lorentzian line profiles.

#### Lifetime width

The inherent lifetime width ( $\Gamma_\tau$ ) stems from the Heisenberg uncertainty principle [3]. An inner-shell vacancy has a finite lifetime ( $\tau$ ) which depends on the transition rates to all possible final states. The lifetime width is inversely proportional to the lifetime as

$$\Gamma_\tau \geq \frac{\hbar}{\tau} \quad (3.3)$$

and the line profile is a Lorentzian.

Non-radiative decay is typically much faster than UV fluorescence decay <sup>1</sup> and a longer lifetime of the fluorescence initial state is reflected as a narrower broadening in a fluorescence spectrum. Photoelectron lines of a valence shell (such as Xe  $5p$  and Ne  $2s$  photolines) have a negligible lifetime broadening for the same reason since for these states the nonradiative decay is energetically forbidden. Therefore valence photolines are often used to evaluate the contribution of other line broadening mechanisms as in Papers I-II, and V.

### Doppler broadening

Especially in experiments where a gas cell is used, the atoms move randomly in the interaction region. The velocity of the atom relative to the analyzer may shift the observed kinetic energy of the ejected electron and the result is called Doppler broadening ( $\Gamma_D$ ). The line profile is a Gaussian and the line width (in meV) depends on the mass of the atom ( $m$  in amu), temperature in the chamber ( $T$  in K), and the kinetic energy of the electron ( $E_{kin}$  in eV) as [44]

$$\Gamma_D = 0.7215 \cdot \sqrt{\frac{E_{kin}T}{m}}. \quad (3.4)$$

Doppler broadening can be diminished by minimizing the velocity component of the atoms in the direction of the analyzer. In other words, a parallel atom beam directed perpendicular to the analyzer needs to be achieved e.g. using a velocity selection [45].

### Spectrometer broadening

In both electron and fluorescence analyzers the finite size of the entrance slit is directly affecting the observed line width. The shape of the spectrometer broadening ( $\Gamma_{sp}$ ) is assumed to be a Gaussian.

### Photon bandwidth

The contribution of the finite photon bandwidth ( $\Gamma_{h\nu}$ ) should not be forgotten either even though it is present only in the photoelectron and resonant Auger spectrum. The normal Auger and UV-fluorescence lines, whose energy does not depend on the excitation energy, are free from this contribution. Photon bandwidth is determined by the monochromator exit slit and its line profile is also a Gaussian.

---

<sup>1</sup>In Kr<sup>+</sup>, a nonradiative decay rate is in the pico or femtosecond range whereas fluorescence decay varies between micro and nanoseconds.

### Total line width

As a result, the total line width of a photoline ( $\Gamma_{tot}$ ) is a convolution (marked with an asterisk) of all above-mentioned contributions

$$\Gamma_{tot} = \Gamma_{\tau} * \Gamma_D * \Gamma_{sp} * \Gamma_{h\nu} \quad (3.5)$$

and Eq. (3.5) was used in Papers I-II, where the lifetime widths  $\Gamma_{\tau}$  were extracted from the experimental total line widths.

Pressure (or collision) broadening caused by collisions of target atoms is not included since it is not an issue with the limited pressures used in the experiments, even though pressure-induced effects were checked in the study of Paper IV. Eq. (3.5) applies also to Auger lines if the photon contribution (the last term) is omitted and the lifetime width ( $\Gamma_{\tau}$ ) represents also the lifetime of the Auger final state.

In case of resonant Auger lines, Eq. (3.5) applies if the photon bandwidth is greater or equal to the lifetime width of the excited state (i.e.  $\Gamma_{h\nu} \geq \Gamma_{\tau}$ ). If the photon bandwidth is substantially smaller, the resulting broadening reflects only the photon bandwidth as observed first by Brown *et al.* [46] and shown theoretically by Åberg and Howat [47]. This line sharpening is due to the Auger resonant Raman effect and the total experimental broadening is equal to

$$\Gamma_{tot} = (\Gamma_{\tau} \cdot \Gamma_{h\nu}) * \Gamma_D * \Gamma_{sp}. \quad (3.6)$$

Figure 3.6 shows how the product (instead of convolution) in Eq. (3.6) reduces the lifetime width in the resonant Raman regime provided that  $\Gamma_{h\nu} < \Gamma_{\tau}$  and resonant Auger lines with subnatural line widths can be observed [48].

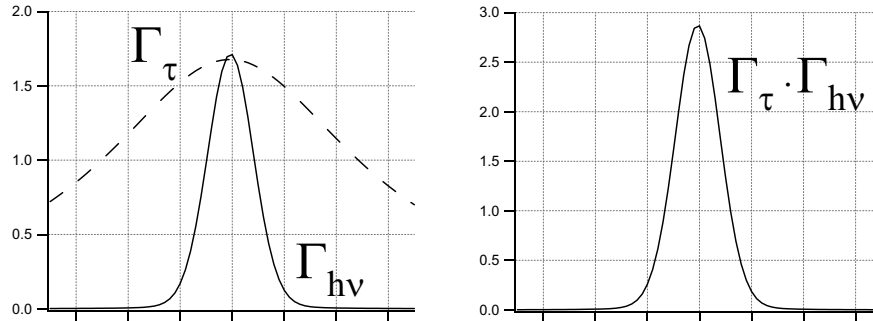


Figure 3.6: Product of the photon bandwidth and the lifetime broadening in case  $\Gamma_{\tau} > \Gamma_{h\nu}$ .



# Chapter 4

## Data analysis

In the course of the measurements, the experimental conditions change. The photon flux decreases exponentially, the pressure in the chamber goes through variations and the transmission of the analyzer alters for different photon or electron energies. Before deriving any results from the experimental data, the effects of possible error sources must be taken into account.

### 4.1 Corrections

Any instrument, whether it is a thermometer, a pressure gauge, an electron spectrometer, or a fluorescence spectrograph, has a finite accuracy. The instruments are calibrated by their manufacturer but under different experimental conditions a recalibration is often needed. Nonetheless, the obtained readings are indicative.

#### 4.1.1 Energy calibration

The wavelength scale of a fluorescence spectrograph as well as the kinetic energy scale of an electron spectrometer needs to be calibrated if accurate wavelengths or energies are wanted. The calibration is made using some well-known lines measured during the experiment and thus under the same experimental conditions. An additional wavelength calibration of the fluorescence spectrograph in Paper IV was unnecessary since the investigated lines themselves are well-known from optical data [14]. A comparison with the known values and the spectrograph readings revealed that the latter ones had shifted approximately 3 nm.

In Papers I-II, where the binding energies of Mn  $3p$  and Eu  $4d$  photolines were determined, a careful energy calibration was essential. In case of Mn (Paper I), the  $3p$  photolines happen to lie close to the well-known Xe  $4d$  photolines [49] and the binding energy calibration was made by measuring an electron spectrum containing both Mn  $3p$  and Xe  $4d$  photolines.

For Eu  $4d$  photolines, there are no suitable photolines nearby. Utilizing the fact that the kinetic energy of photolines is a linear function of exciting photon energy [cf. Eq. (2.6)] and the kinetic energy of Auger lines is always the same, the unknown photolines can be shifted to overlap partially with known Auger lines [e.g. Xe  $N_{4,5}O_{2,3}O_{2,3}$ <sup>1</sup> Auger lines [50]]. This way one obtains the correct kinetic energies of the photolines but before applying Eq. (2.6) the used photon energy also requires a calibration with a known photoelectron line (such as Xe  $4d$  used in Paper II).

When performing experiments requiring a resonant excitation such as the resonant Auger studies in Papers III-V, the correct excitation energy has to be found by measuring an absorption spectrum (in practice, a total ion or electron yield, see Fig. 2.3). The energy of photons passing through the monochromator exit slit shifts as the optical elements are warmed up under the radiation exposure. Therefore, in the study of Paper V, the exact position of the resonance was checked from time to time in order to measure with a photon energy exactly on top of the Ne  $1s \rightarrow 3p$  resonance.

### 4.1.2 Transmission correction

In Papers I-II, electron spectra were measured over a range of several dozens of eVs. This requires considerable changes in the voltages of the retarding lens and produces variations in the transmission of the electron analyzer. Typically, the transmission decreases as a function of the kinetic energy but due to different experimental conditions, a transmission correction should be made each time the experimental parameters have been modified, especially if the relative intensities of the electron lines are to be compared with one another or with calculated values. By observing the intensity ratio between a photoline and the subsequent Auger lines at different photon energies the transmission of the spectrometer can be deduced [51]. In Papers I-II, the Xe  $4d$  photolines were followed as a function of the photon energy and compared with selected Xe  $N_{4,5}O_{2,3}O_{2,3}$  Auger lines.

### 4.1.3 Detector efficiency

The detection of electrons in SES-100 and SES-200 analyzers is carried out by scanning an electron peak across the detector and summing the intensity from each channel together. Consequently, deficiencies in some channels do not contribute to the final outcome.

However, the fluorescence spectrograph used in Paper IV utilizes so-called fixed mode to record a wavelength interval  $\lambda + \Delta\lambda$  and in the course of the data analysis few of the channels were found to give only a zero contribution. In order to compensate efficiency changes, a strong fluorescence line was

---

<sup>1</sup>Notation  $N_{4,5}O_{2,3}O_{2,3}$  is equal to  $4d^{-1} \rightarrow 5p^{-2}$ .

scanned across the CCD detector. The intensity of the line at different points of the detector provided the variations in the efficiency after accounting for the decreased photon flux during the measurements.

#### 4.1.4 Variations in experimental conditions

During a measurement, the experimental conditions should be kept constant. Any optimization required is made in advance to avoid sudden changes that might alter the results. However, not all parameters can be kept constant and one of these is the photon flux.

In Papers III-IV, the photon energy was scanned across the Kr  $3d \rightarrow np$  ( $n = 5, 6$ ) resonances. Tuning the photon energy has an influence on the photon flux that has to be taken into account. Therefore, the reading of the photodiode current, which measures the flux behind the interaction region, was recorded and used in the data analysis to normalize the flux variations.

Another fluctuating parameter in gas phase experiments is the chamber pressure. In normal conditions, the pressure is approximately constant over time but it has to be monitored for unexpected changes that might endanger the ultra-high vacuum of the monochromator.

## 4.2 Data processing

In order to extract information from an experimental spectra, the spectra is fitted with analytical curves characterized by a peak position, an intensity, a Lorentzian and a Gaussian line width component, and an asymmetry parameter. The sum of these curves constitutes an envelope and the goodness of the fit can be evaluated by calculating the square of the differences between the data points ( $Y_i$ ) and the value of the envelope at that point ( $y_i$ ) [i.e.  $(Y_i - y_i)^2$ ]. The optimal result is achieved by minimizing this quantity as the peak positions, intensities, widths, and asymmetries are varied under the restrictions given beforehand.

As a result of this fitting procedure, the characteristics of the spectral lines (energy, intensity, width components, and possible asymmetry) are obtained. Comparing the intensity obtained from measurements at different angles, the angular distribution parameter can be calculated according to Eq. (2.13) for the ejected electron as well as for the emitted fluorescence. The normalization of the spectra from different angles relative to each other usually requires that one (or more)  $\beta$  parameter is known. In Paper V, the spectra were normalized with the help of ( $^1D$ ) $3p^2D$  ( $\beta = -0.99$ ) and  $2s$  photoline ( $\beta \approx 2$ ).

As described before, the total line width is composed of a Lorentzian and a Gaussian line profile. The only Lorentzian contribution comes from the inherent lifetime width. By estimating the magnitude of the other broadenings

in Eq. (3.5) (i.e.  $\Gamma_D$ ,  $\Gamma_{sp}$ , and  $\Gamma_{hv}$ ) the Lorentzian component of the total width can be extracted by fixing the Gaussian component and running the fitting procedure. This was applied in Papers I-II where the lifetime widths of Mn  $3p$  and Eu  $4d$  photolines were obtained.

### 4.3 Deconvolution

In case of a line group that has large line widths and small energy separations between the lines, the individual lines are smeared out, which complicates the interpretation of the spectrum. Since the experimental conditions are the same for each of the lines, the line broadenings resulted from the Doppler effect, the spectrometer, and the photon band are also the same. By deconvolving these contributions from the spectrum, the resolution enhances and individual lines are better resolved.

Deconvolution is an inverse process of convolution. In practice, obtaining a functional deconvolution program is not a trivial task due to experimental background noise. If the noise is handled appropriately, the deconvoluted spectrum might reveal features not observed before. Otherwise, the only benefit of the procedure is visual.

In Paper V, the deconvolution program RECOVERY [52] was tested. The program is based on a maximum likelihood method, which provides the ultimate resolution enhancement compared with any other non-parametric methods or with linear methods. The goal of the program is to determine the estimate of the unknown function (i.e. signal) as accurately as possible from the random function (i.e. the measured spectrum). In the computations of the required convolutions, RECOVERY exploits a fast Fourier transform program.

# Chapter 5

## Calculations

The relativistic atomic structure calculations performed in all included papers are based on the multiconfiguration Dirac-Fock (MCDF) method. These *ab initio* calculations are derived from relativistic quantum mechanics without reference to any empirical data. Consequently, while they provide a basis for the interpretation of the experimental data, they also serve as a validity test of quantum mechanics. Nowadays, even after decades of testing, quantum mechanics is considered to be the best description we have for atoms.

### 5.1 Wave functions and energies

The MCDF method originates from the time-independent Schrödinger equation [2]

$$H\Psi = E\Psi, \quad (5.1)$$

where the state of the system (in this case an atom) is described by a wave function  $\Psi$ ,  $H$  is the Hamiltonian operator for the system, and  $E$  the total energy. For a system with  $N$  electrons, the Dirac-Coulomb Hamiltonian utilized in the relativistic MCDF method is of the form (in atomic units)

$$H_{DC} = \sum_{i=1}^N [c\boldsymbol{\alpha}(i) \cdot \mathbf{p}(i) + \beta(i)c^2 + V(\mathbf{r}_i)] + \sum_{i<j}^N \left| \frac{1}{\mathbf{r}_i - \mathbf{r}_j} \right|, \quad (5.2)$$

where  $\mathbf{r}_i$  is the position vector of an electron  $i$ ,  $c$  is the velocity of light,  $\boldsymbol{\alpha}(i)$  and  $\beta(i)$  are the Dirac matrices, and  $\mathbf{p}(i)$  is the momentum operator. The first sum includes the one-electron Dirac Hamiltonians in the spherical potential energy  $V(\mathbf{r}_i)$  and the latter sum represents the interactions amongst the electrons. [53, 54]

In practice, the calculation of the Coulomb repulsion between the electrons is first evaluated in the central-field approximation by an average screening of the stationary nuclear charge and the solutions  $\Psi$  are found

by varying the total energy ( $E = \langle \Psi | H | \Psi \rangle$ ) as long as a stationary solution is obtained [53]. Subsequently a more accurate estimate of Coulomb interaction is obtained by configuration mixing.

Dirac orbitals, which are solutions of the one-electron Dirac equation [55], are of the form

$$\psi_{n\kappa m}(\mathbf{r}) = \frac{1}{r} \begin{bmatrix} P_{n\kappa}(r) & \chi_{\kappa,m}(\theta, \phi) \\ iQ_{n\kappa}(r) & \chi_{-\kappa,m}(\theta, \phi) \end{bmatrix}, \quad (5.3)$$

where  $m = m_j$ ,  $P_{n\kappa}(r)$  and  $Q_{n\kappa}(r)$  are radial functions,  $\chi_{\kappa,m}(\theta, \phi)$  are spin-orbit functions, and  $\kappa$  is the relativistic quantum number [ $\kappa = -2(j-l)(j + \frac{1}{2})$ ]. Using these one-electron orbitals, antisymmetrical Slater determinants are formed for an  $N$  electron atom as

$$\Psi = \frac{1}{\sqrt{N!}} \det |\psi(1)\psi(2)\cdots\psi(N)|. \quad (5.4)$$

These determinant functions could be used, but instead, coupled wave functions, which are more concise, are used in calculations. [54]

In the relativistic atomic structure program GRASP92 [56], a configuration state function (CSF)  $\Psi^{CSF}$ , which is characterized by specific values of  $\Pi$ ,  $J$ , and  $M_J$ , is constructed from the one-electron orbitals in the  $jj$ -coupling scheme. The  $jj$ -coupled wave function can be expanded to linear combinations of uncoupled Slater determinants [57] if needed in numerical computations of e.g. transition probabilities of radiative transitions.

An atomic state function (ASF)  $\Psi^{ASF}$ , describing an atomic state with given  $J$  and  $\Pi$ , is a linear combination of the CSFs

$$\Psi^{ASF} = \sum_{i=1}^{n_C} c_i \Psi_i^{CSF}, \quad (5.5)$$

where  $c_i$  are mixing coefficients and  $n_C$  is the number of CSFs included. If more than one configuration is used in the formation of the CSFs the mixing of these configurations via mixing coefficients  $c_i$  is called configuration interaction (CI). A calculation with only one configuration is referred to as single-configuration (SC) approximation, whereas two or more configurations make up a multiconfiguration (MC) calculation. Especially in Paper I the effects of CI were studied by comparing the results of SC and MC calculations.

If the orbital wave functions are fixed, the solving of the ASFs and corresponding eigenenergies is reduced to a set of equations

$$(H - E_j I)c_j = 0, \quad (5.6)$$

for each state  $j$ . Above,  $c_j$  is the  $j$  component of a vector with  $n_C$  components,  $I$  is a  $n_C \times n_C$  unit matrix, and  $H$  is the Hamiltonian operator

matrix. Orbitals and mixing coefficients can be optimized self-consistently either separately, when it is called an average-level (AL) calculation (uses an average energy of the configuration in orbital optimization) or together, which is known as an (extended-)optimal level [(E)OL] calculation [uses the energy of one (or more) specified ASF].

## 5.2 Transition probabilities

The wave functions and energies obtained from GRASP92 have been used in Papers I-V to calculate transition probabilities and angular distribution parameters. In the sudden approximation [58], the transition is considered to be an abrupt change in the potential but the initial ( $\Psi_i$ ) and final states ( $\Psi_f$ ) can be assumed to be well defined.

Calculation of any property related to a transition stems from the transition amplitude

$$T_{if} = \langle \Psi_f | V | \Psi_i \rangle, \quad (5.7)$$

where the transition between the initial and final states is mediated by an operator  $V$ . If an electron is emitted in the transition, the final state consists of the continuum electron ( $\varepsilon l$ ) and the final state of the atom ( $\phi_f$ ) i.e.  $|\Psi_f\rangle = |\phi_f \varepsilon l\rangle$ .

The transition probability (or rate)  $P_{if}$  of a selected transition is proportional to the square of the transition amplitude [59]

$$P_{if} = \frac{2\pi}{\hbar} |T_{if}|^2. \quad (5.8)$$

This is also known as Fermi's golden rule.

### 5.2.1 Photon-atom interaction

In a direct photoionization, the photon-atom interaction leads to an emission of an electron. The photon is described as an electromagnetic wave  $\mathbf{A} \propto \hat{\mathbf{e}} \cdot \exp(i\mathbf{k} \cdot \mathbf{r})$ , with the characteristic polarization vector of the field ( $\hat{\mathbf{e}}$ ), wave number vector ( $\mathbf{k}$ ), and the position vector of the wave ( $\mathbf{r}$ ). In dipole approximation, only the first term of the Taylor expansion

$$e^{i\mathbf{k} \cdot \mathbf{r}} = 1 + i\mathbf{k} \cdot \mathbf{r} - \frac{1}{2}(\mathbf{k} \cdot \mathbf{r})^2 + \dots \quad (5.9)$$

is taken into account. This reduces the photon-atom interaction to  $V_D = \sum_i \mathbf{p}_i \cdot \mathbf{A} \propto \sum_i \mathbf{p}_i \cdot \hat{\mathbf{e}}$ . The momentum of the electron can be expressed either as  $\mathbf{r}_i$  (in the length form) or as  $-i\hbar\nabla_i$ <sup>1</sup> (in the velocity form) [60]. The

---

<sup>1</sup>In atomic units,  $\hbar = 1$ .

length and velocity forms of the transition amplitude are, however, exactly equal for exact eigenfunctions of the many electron Hamiltonian only. In approximative calculations, the length and velocity forms are equal if relaxation is neglected for one electron orbitals, calculated in local potentials.

In Papers I-II, the photoionization transition probabilities were approximated by a program called PHOTION<sup>2</sup> [61], which exploits the ASFs obtained from GRASP92 for the initial ( $i$ ) and final ionic states ( $f$ )

$$\Psi_i^{ASF} = \sum_{\alpha} c_{i\alpha} \Psi_{\alpha}^{CSF}(J_i), \quad \Psi_f^{ASF} = \sum_{\beta} c_{f\beta} \Psi_{\beta}^{CSF}(J_f). \quad (5.10)$$

By comparing the mixing coefficients ( $c_{i\alpha}$  and  $c_{f\beta}$ ) and multiplying the coefficients with the same parent configuration together, the transition probability is obtained by taking a square of the multiplied coefficients summed together and multiplying the square with an angular momenta dependent weight factor  $\Lambda(J_i, j_{\mu}, J_f)$ . In other words,

$$T_{if}^{PI} = \Lambda(J_i, j_{\mu}, J_f) \left| \sum_{\alpha\beta} c_{\alpha i} c_{\beta f} \delta_{X_{\alpha} Y_{\beta}} \right|^2, \quad (5.11)$$

where  $j_{\mu}$  is the momentum of the ionized orbital,  $X_{\alpha}$  refers to the configuration associated with the final ionic state and  $Y_{\beta}$  to the same parent configuration in the initial state [62]. This approximation does not provide any information about the photoelectron but, in the light of the results in Papers I-II, it is sufficient for providing a rough estimation. The results of this program also indicate if the ASFs<sup>3</sup> are poor by giving a result far from the one observed.

The resonant Auger final states  $4p^{-2}np$  in Kr studied in Papers III-IV are also populated via direct photoionization. To study the interference between different population mechanisms in Paper III the direct photoionization amplitudes were calculated using a new PHOTO component [63] of the RATIP package [64]. PHOTO utilizes the nonorthogonality of separately optimized orbitals in the initial and final states of the transition and gives the results both in the length (also known as Babushkin) and in the velocity (also known as Coulomb) gauges.

In Papers III-IV, photoabsorption (or excitation) probabilities were also calculated using a program called REOS99 [65], which requires that the ASFs are expanded to a determinant basis with its accompanying component CESD99 [57].

## 5.2.2 Coulomb interaction

In Papers I-II, and V, the Auger decay has been treated as a simplified two-step process in which the Auger decay from an ionized or excited state is

<sup>2</sup>Nowadays, the revised version of this program is known as IONIS.

<sup>3</sup>actually, the mixing coefficients of the ASFs

considered to be a separate and independent event. In this approximation, the transition probability is simply proportional to the square of the transition amplitude in Eq. (5.7) with the Coulomb interaction operator ( $V = V_C$ ), i.e.

$$T_{if}^A = \langle \Psi_f | \sum_{i < j} \frac{1}{r_{ij}} | \Psi_i \rangle. \quad (5.12)$$

In the frozen core approximation, all but the participating subshells are assumed to be left unchanged during the transition  $n_b l_b^{-1} \rightarrow n_c l_c^{-1} n_d l_d^{-1} + \varepsilon_A l_A$  and Eq. (5.12) is reduced to a two-electron matrix element that in turn can be calculated with the help of Slater integrals as

$$\begin{aligned} \left\langle bA; JM \left| \frac{1}{r_{12}} \right| cd; J'M' \right\rangle &\propto \sum_k \int_0^\infty \int_0^\infty [P_b(1)P_c(1) + Q_b(1)Q_c(1)] \\ &\times [P_A(2)P_d(2) + Q_A(2)Q_d(2)] \frac{r_{<}^k}{r_{>}^{k+1}} dr_1 dr_2, \end{aligned} \quad (5.13)$$

where  $P_{nl}(r)$  and  $Q_{nl}(r)$  are radial wave functions and the notation  $r_{<}$  ( $r_{>}$ ) is used for  $\min(r_1, r_2)$  [ $\max(r_1, r_2)$ ]. [34]

The Auger decay rates ( $\propto |T_{if}^A|^2$ ) in Papers I-II have been computed by utilizing a program called AUGER [66] which also provides the  $\beta$  parameters of Auger electrons if requested as in Paper V. The program can also print the radial integrals, a feature which was utilized in Paper I. The SC calculation predicted too pronounced super-Coster-Kronig decay rates whereas in the MC approximation these decay rates were contracted. A closer inspection of radial integrals revealed that this was due to a cancellation of amplitude components with different signs.

If the calculated Auger decay spectrum is plotted as in Papers I-II, the Auger decay rates ( $P_{jf}^A$ ) have to be multiplied with the photoionization probabilities of the intermediate state  $j$  ( $P_{ij}^{PI}$ ) and divided by the total decay rate ( $\sum_j P_{jf}$ ) i.e.

$$N_A = \frac{P_{jf}^A P_{ij}^{PI}}{\sum_j P_{jf}}, \quad (5.14)$$

where  $N_A$  is the number of electrons [61].

The calculations performed with AUGER are limited to transitions involving two-electrons only [cf. Eq. (5.13)]. This excludes the calculation of shake-up (or down) transitions including three active electrons, which actually sometimes are dominating transitions in resonant Auger decay [20].

The probabilities of resonant Auger transitions including a shake process  $nl \rightarrow n'l'$  ( $n \neq n'$ ) can be evaluated in the strict spectator approximation [67] according to which the interaction between the spectator electron and core electrons is so weak that it can be ignored. Then the amplitude of a transition  $\phi_i nl \rightarrow \phi_f n'l'$  can be expressed in a simplified form [68]

$$\langle \phi_f n'l' | V_C | \phi_i nl \rangle \approx \langle n'l' | nl \rangle \langle \phi_f nl | V_C | \phi_i nl \rangle, \quad (5.15)$$

where  $\phi_{i(f)}$  is the initial (final) state configuration without the excited electron and  $\langle n'l'|nl\rangle$  represents the overlap integral of the orbitals  $n'l'$  and  $nl$ .

As a result, for a specific final state  $\phi_f n_k l_k$ , the transition amplitude from an initial state  $\phi_i nl$  can be expressed as

$$\langle \phi_f n_k l_k | V_C | \phi_i nl \rangle \approx \sum_{n'} \langle n_k l_k | n'l' \rangle \langle \phi_f n'l' | V_C | \phi_i nl \rangle, \quad (5.16)$$

where the summation includes the case  $n'l' = nl$  as well and has a restriction  $\sum_{n_k} \langle n_k l_k | n'l' \rangle = 1$ . The right side of the equation is non-zero also for cases  $n'l' \neq nl$  if configuration interaction is included and it mixes the configurations considerably. This was the case for Kr  $4p^4 np$  ( $n \geq 5$ ) states in Papers III-IV.

### 5.2.3 Resonant photoionization

The two-step formalism has been considered to be adequate also in the description of resonant Auger decay provided that the photon energy is chosen from the top of an isolated resonance [69]. In case of close-lying resonances with large lifetime widths that overlap, the two-step approximation is no longer valid and the interference between these two channels ( $i \rightarrow R_1 \rightarrow f$  and  $i \rightarrow R_2 \rightarrow f$ ) is observed [70].

The transition amplitude between the initial and final states  $\Psi_i$  and  $\Psi_f$  when accounting for resonance channels via excited states  $\Psi_R$  is expressed as [47]

$$T_{if}^{RA} = \langle \Psi_f | V_D | \Psi_i \rangle + \sum_R \frac{\langle \Psi_f | V_C | \Psi_R \rangle \langle \Psi_R | V_D | \Psi_i \rangle}{h\nu - E_R + i\Gamma_R/2}, \quad (5.17)$$

where  $\Gamma_R$  and  $E_R$  are the lifetime width and energy (relative to the initial state) of the resonance  $R$ . The first term of the expression is the direct photoionization mediated by a dipole operator ( $V_D$ ), whereas the summation represents the resonance contribution, which can be computed in the two-step formalism. The photoexcitation amplitude  $\langle \Psi_R | V_D | \Psi_i \rangle$  can be calculated using REOS99 and the subsequent Auger amplitude  $\langle \Psi_f | V_C | \Psi_R \rangle$  using AUGER.

On top of a resonance  $R$  only one term of Eq. (5.17) dominates and the use of the two-step model is justified. However, if the direct contribution is large, the interference between the direct and the resonant channel has to be taken into account. In case of two overlapping resonances, as the  $3d_{3/2}^{-1}5p$  and  $3d_{5/2}^{-1}6p$  resonances in Kr (see Fig. 2.3) investigated in Papers III-IV, the interference between the resonance channels, which is also called coherence, needs to be taken into account.

Interference can be seen as asymmetric line shapes, also known as Fano profiles, of the intensity as a function of photon energy [71]. However, the interference seen in the intensities is sometimes rather subtle since it is proportional to the square of the transition amplitude. Instead, the  $\beta$  parameters

are calculated from the transition amplitudes as a coherent sum and they therefore contain more direct information about the phase differences of the contributing channels (or partial waves), which are responsible for interference effects [72]. Therefore, a complete experiment that provides the relative amplitudes and their phases (and all the other information of the decay) requires the determination of the  $\beta$  parameter (and spin-polarization) of the electron [73]. For Xe, a complete experiment has been performed by combining the data of  $\beta$  parameters and spin-polarization of the electron with the alignment of the ion obtained from PIFS measurements in a resonant Auger decay  $4p_{5/2}^{-1}6p \rightarrow 5p^46p$  [74].

In Papers III-IV, the interference was investigated at the Kr  $3d \rightarrow np$  resonances with the MCDF calculations. The public RATIP package lacks a code calculating the direct amplitudes, which had prevented this kind of computations from us until then. Others had already performed interference calculations earlier, Sorensen *et al.* in 1994 [75] and Lagutin *et al.* [76] more recently.



# Chapter 6

## Summary of the included papers

The history of both electron and fluorescence spectroscopy can be divided into two eras: the time before and the time after synchrotrons. The possibilities of the era after synchrotrons have increased the number of experiments in both of these fields and, most of all, they have enhanced the scope of accessible problems. As said before, the high-resolution photoelectron studies of metal vapours (Papers I-II) could not have been done without the high flux of synchrotron radiation. On the other hand, it is the tunability and small bandwidth of synchrotron radiation that has made resonant Auger studies in the Raman regime (Papers III-V) possible.

The latter era also brought new challenges for theoreticians. A great many new experimental observations were achieved with a better resolution that required more accurate or completely new theoretical predictions. At the same time, the computational power of computers has increased providing the necessary tools for performing the required calculations.

This thesis consists of five original papers which all include an experimental part obtained using synchrotron radiation and a theoretical part with new calculations. In the following, the motivation and the results of these papers are briefly summarized.

### Papers I-II: Metal vapours

A decade ago, the third generation synchrotron light source MAX-II was built. Soon after, the first measurements were performed at the beamline I411 [33] and among them, some electron spectra of atomic Mn were measured. One of the several photoelectron and Auger spectra contained both the  $3p$  photoelectron spectrum and the subsequent Auger spectrum that looked like a mirror image of the photoelectron spectrum. This feature persuaded us to perform new measurements concentrated on the  $3p$  photoionization and its

Auger decay.

There are several earlier studies of the Mn  $3p$  photoelectron spectrum which have been reviewed recently by Martins *et al.* [77]. One of these studies [78] had already investigated the  $3p$  photoelectron spectrum in detail together with the calculations from the Cowan code [4]. The studies on the Auger decay following the  $3p$  photoionization are far more rare and they have been measured with a rather moderate resolution. To demonstrate this, Fig. 6.1 shows the results obtained by Väyrynen and Aksela in 1981 [79] and the ones published in Paper I.

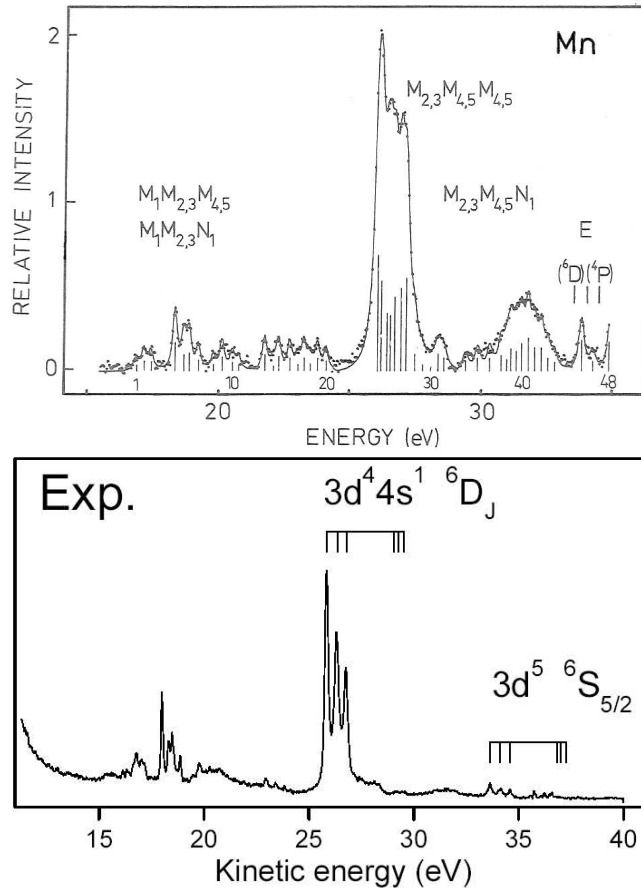


Figure 6.1: Auger spectra of Mn measured using electron bombardment (upper panel)[79] and synchrotron radiation (lower panel).

The data analysis revealed that the most prominent Auger lines (around  $E_K \approx 25 - 28$  eV) are slightly broader than the most prominent photolines corresponding to the initial states of these Auger transitions. Our computations showed that this was indeed the case. The three lines in the Auger spectrum originated from transitions  $3p^5(^2P)3d^5 4s^2 ^7P_J \rightarrow 3d^4 4s^1 ^6D_{J'}$  (where  $J = 4, 3, 2$  and  $J' = 9/2 - 1/2$ ) and were composed of a group of final states

instead of one final state explaining the broader structure.

Followed by the success of our calculated Auger spectrum in MC approximation, the Eu  $4d$  photoionization and the subsequent Auger spectrum were measured in order to perform a similar study. These measurements provided us the same information as the ones of Mn: the experimental binding energies, intensity ratios, and lifetime widths of the most prominent photolines with higher accuracy than earlier [78, 80].

However, the calculations for Eu became considerably more complicated. Whereas the CSF basis for an extended calculation of a rare gas atom has some dozens of states and the MC calculation for Mn performed in Paper I consists of several hundreds of states, a SC calculation for some Auger final states in Eu deals with thousands of states. Even though the most prominent features of the  $4d$  photoelectron spectrum of Eu were very well reproduced by our rough photoionization approximation (as was the case also in Mn), the desire to compare the calculated Auger spectra obtained from the SC and MC approximations had to be buried.

In Mn (Paper I), the initial ionic state configuration interaction (IISCI) was found to be in a major role in reproducing the Auger spectrum. In the  $LS$ -coupling scheme, super-Coster-Kronig transitions from the  $3p^{-1}{}^7P_J$  states to the  $3d^{-2}$  final states are completely forbidden. The  $jj$ -coupling scheme does not propose such a restriction and in SC approximation, the super-Coster-Kronig transitions were overestimated judging by the comparison with experimental spectrum. In the MC approximation, the mixing of the  $3p^53d^54s^2$ ,  $3p^53d^64s^1$ , and  $3p^53d^7$  configurations (IISCI) resulted in a reduction in the transition probabilities to the  $3d^{-2}$  final states in accordance with the observed spectrum. Thus, Auger decay was found to be a more sensitive tool for investigating the computational details than photoionization.

Due to the restricted computational feasibility, only few of the Auger transitions following the Eu  $4d$  photoionization could be analyzed. However, in the light of the obtained calculations, the most prominent features in the Auger spectrum can be attributed to Coster-Kronig transitions to the  $4f^{-1}5p^{-1}$  and  $4f^{-1}5s^{-1}$  final states (structures around  $E_K = 88$  eV and  $65 - 70$  eV, respectively).

### Paper III-IV: Interference effects in Kr

Among the first experiments performed at the brand-new beamline I411 were also the angle-resolved measurements of the Kr  $4p^4({}^1D)np$  ( $n = 5, 6$ ) states across the overlapping  $3d_{3/2}^{-1}5p$  and  $3d_{5/2}^{-1}6p$  resonances. This study aroused from the earlier observations of the lifetime interference (or coherence) between these resonances in the intensities of these line groups [70]. However, the obtained experimental results lacked a theoretical counterpart for several years.

In the meantime, PIFS measurements of the alignment parameters became popular (see e.g. [81]) and the alignment of the resonant Auger final states  $4p^4 5p$  was investigated a great deal [82]. The experiments were first confined to specific energies at the top of the resonances and interpreted with the help of the two-step calculations, which was also the evolution of the Auger electron  $\beta$  parameter studies of the Kr  $4p^4 5p$  states [83]. During the past five years, the alignment studies have been extended to cover several energies across the  $3d \rightarrow np$  ( $n = 5, 6$ ) resonances and all the channels in Eq. (5.17) have been included in the Pauli-Fock calculations [76, 84].

Published in 2007 [85], the photon energy-dependency of the  $\beta$  parameters across the  $2p \rightarrow 3d, 4s$  resonances in Ar were calculated within the MCDF theory. Soon after, similar calculations were also performed for Kr in order to interpret the above-mentioned experimental results (Paper III) as well as the new results from PIFS measurements performed in 2006 (Paper IV).

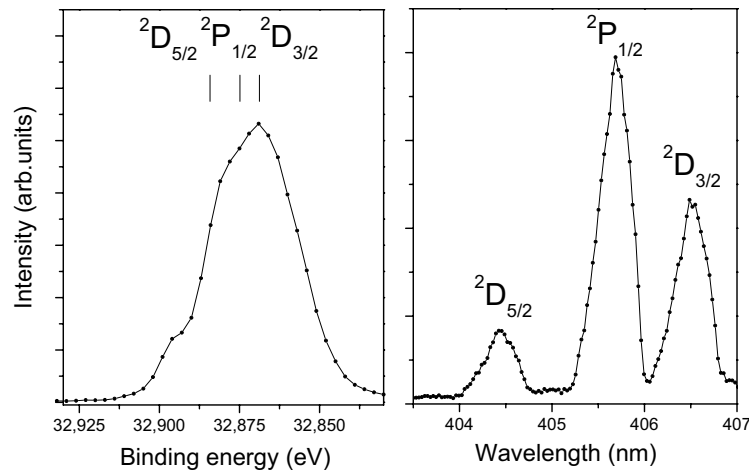


Figure 6.2: Electron and fluorescence spectra of  $4p^4(^1D)5p$   $^2D_{5/2}$ ,  $^2P_{1/2}$ , and  $^2D_{3/2}$  states.

As mentioned earlier, the  $\beta$  parameters of Auger electrons (as well as the alignment parameters) are far more sensitive to interference effects than intensities [72], which is evident from the results of Paper III. The experimental  $\beta$  values show very pronounced variations especially for the  $4p^4(^1D)6p$  states as the photon energy is scanned across the  $3d_{3/2}^{-1}5p$  and  $3d_{5/2}^{-1}6p$  resonances. Unfortunately, the PHOTO package was unable to predict any direct contribution for states with  $J > 3/2$ , even though these lines have also been observed outside the resonances as in the fluorescence spectra of Paper IV. The lack of direct contribution was clear from the difference between the calculated and measured behaviour of the  $\beta$  parameter for one line, where the only contributing channels were via the  $3d_{3/2}^{-1}5p$  resonance and direct photoionization. In contrast, for another line the  $3d_{5/2}^{-1}6p$  resonance channel had

a major contribution as well and the correspondence between the experimental and calculated  $\beta$  parameter enhanced greatly when the shake transitions were accounted for and the lack of the direct contribution was not so evident.

The experimental resolution in Paper III was less than 30 meV but it was not sufficient for separating all the  $(4p^4(^1D)5p, 6p)$  states. For example, line 1 was a superposition of three final states ( $^2D_{5/2}$ ,  $^2P_{1/2}$ , and  $^2D_{3/2}$ ). Fascinated by the outmost resolution of PIFS measurements, the fluorescence emitted from these states was measured and even though the experimental resolution was a compromise between the resolution and the transmission, these lines were resolved easily. Figure 6.2 shows these lines measured with the electron spectrometer (SES-200) and with the fluorescence spectrograph.

However, since the fluorescence measurements were performed in the plane of the electric vector of incident photons, the results were angle-dependent. In other words, the intensity varies as a function of the photon energy due to the changes in the  $\beta$  parameter. Another reason which complicates the interpretation of the intensity ratios is the cascade contribution from higher-lying states. The transition scheme related to this problem is sketched in Fig. 6.3.

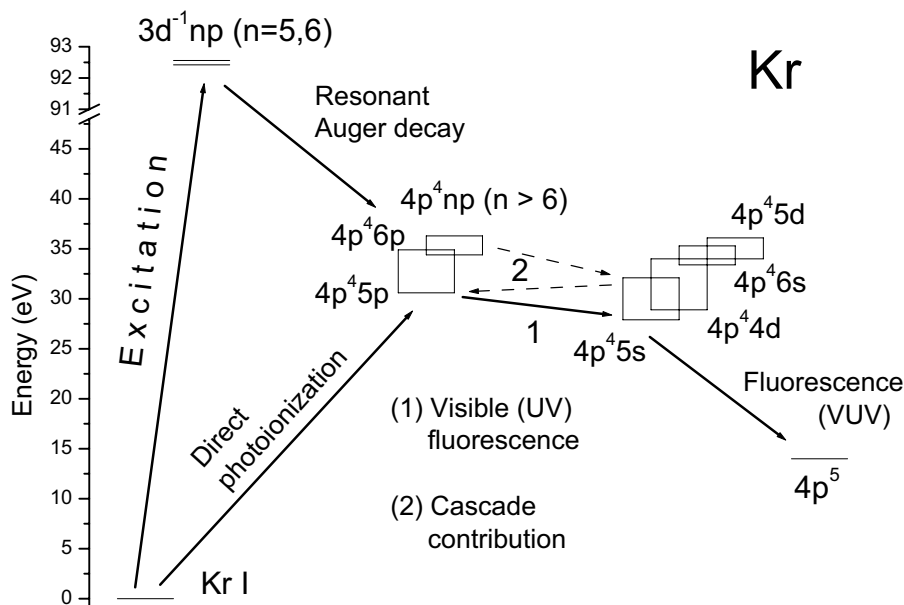


Figure 6.3: Transition scheme of the population and the subsequent decay of the Kr  $4p^4 5p$  states.

Due to the minor outcome from the experimental side in Paper IV, an extended set of calculations was performed. Again, the initial state configuration interaction (ISCI) was found to be important. The inclusion of  $7p$  orbitals both in the initial and final states did not affect the composition of

the final states much but changed the mixing coefficient of the initial states considerably. Consequently, the Auger amplitudes were changed and a reversed interference in the intensity behaviour, in contrast with the earlier calculations and the experimental results, was observed.

## Paper V: Resolution enhancement

The resonant Auger decay following the  $1s \rightarrow 3p$  excitation in Ne has also been the subject of several investigations [19, 86]. However, the photon energy needed to excite the  $1s$  electron to the  $3p$  subshell is about 867 eV and with a  $5 \mu\text{m}$  monochromator exit slit, the photon bandwidth is approximately 200 meV at the beamline I411. In addition, the Doppler broadening for Ne with large kinetic energies ( $E_K > 800$  eV) is greater than 80 meV. Consequently, the observed resonant Auger lines are broad.

Beamline 27SU [87] at the synchrotron facility SPring-8 offers a possibility to reduce the photon bandwidth below 100 meV at  $h\nu = 867$  eV. In such a case, the Doppler contribution becomes an important factor in the total width. To overcome this broadening, the Doppler-free measurements were performed by restricting the motion of neon atoms [45]. Using a parallel atom beam eliminates the Doppler broadening but decreases the intensity in comparison with the gas cell measurements.

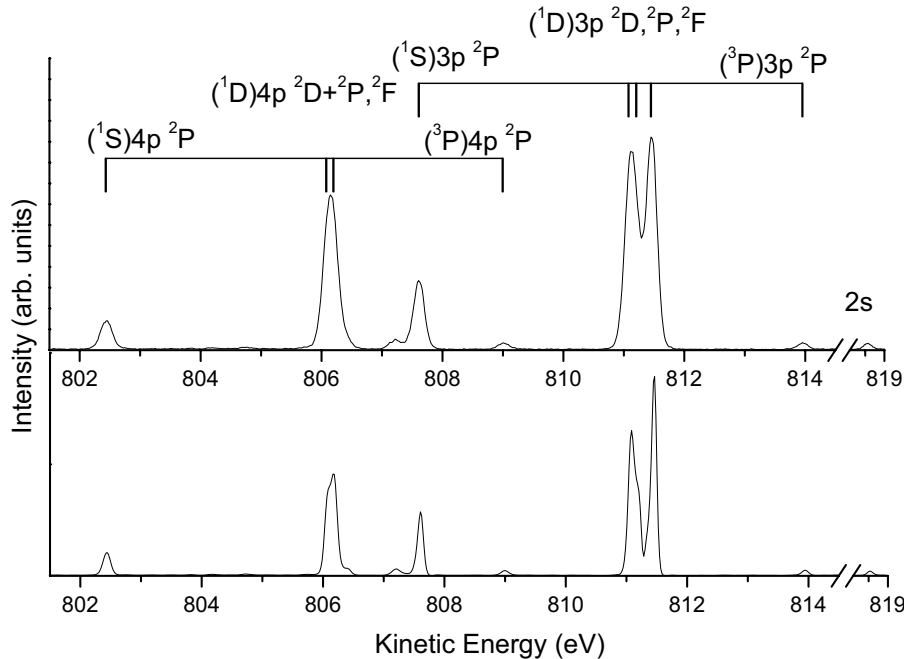


Figure 6.4: Original (upper panel) and deconvolved (lower panel) resonant Auger spectrum following the Ne  $1s \rightarrow 3p$  excitation.

The resolution at the beamline I411 could also be enhanced by using a gas jet and restricting the photon bandwidth. However, obtaining sufficient statistics with these settings would increase the recording time out of reasonable range. Therefore, the resolution enhancement applied afterwards was a tempting alternative.

Figure 6.4 shows the angle-independent resonant Auger spectrum after  $1s \rightarrow 3p$  excitation. The spectra measured with three different angles were deconvoluted with different broadenings. To demonstrate the result of the deconvolution, a deconvoluted spectrum is shown in the lower panel of Fig. 6.4. The  $\beta$  parameters were determined from the original and deconvoluted spectra to ensure no information loss occurred in the deconvolution process. The  $\beta$  parameters were compared with calculated and previously published values [86] which showed that the deconvolution is a practicable tool for resolution enhancement.



# Bibliography

- [1] M. Planck, *Ann. d. Phys.* **4**, 553 (1901).
- [2] E. Schrödinger, *Ann. d. Phys.* **79**, 361 (1926); E. Schrödinger, *Ann. d. Phys.* **79**, 489 (1926); E. Schrödinger, *Ann. d. Phys.* **80**, 437 (1926); E. Schrödinger, *Ann. d. Phys.* **81**, 109 (1926).
- [3] W. Heisenberg, *Z. Physik* **43**, 172 (1927).
- [4] R.D. Cowan, *The Theory of Atomic Structure and Spectra*, (University of California Press, Berkeley, 1981).
- [5] J.J. Thompson, *Philosophical Magazine* **44**, 293 (1897).
- [6] A. Beiser, *Concepts of Modern Physics*, (McGraw-Hill, Inc., New York, 1995).
- [7] W. Pauli, *Z. Physik* **31**, 765 (1925).
- [8] W.C. Martin and W.L. Wiese in *Atomic, Molecular, & Optical Physics Handbook*, Ed. G.W.F. Drake (American Institute of Physics, New York, 1996).
- [9] H. Hertz, *Ann. d. Phys.* XXXI, 983 (1887).
- [10] A. Einstein, *Ann. d. Phys.* **17**, 132 (1905).
- [11] O.-P. Sairanen, A. Kivimäki, E. Nömmiste, H. Aksela, and S. Aksela, *Phys. Rev. A* **54**, 2834 (1996).
- [12] V. Schmidt, *Electron Spectrometry of Atoms using Synchrotron Radiation*, (Cambridge University Press, Cambridge, 1997).
- [13] J.M. Hollas, *Modern Spectroscopy*, (Wiley, New York, 1999).
- [14] C.E. Moore, *Atomic Energy Levels*, (U.S. GPO, Washington, D. C., 1971), Vol. II; A.R. Striganov and N.S. Sventitskii, *Tables of spectral lines of neutral and ionized atoms*, (Plenum, New York, 1968); NIST Atomic Spectra Database (<http://physics.nist.gov/PhysRefData/ASD>).

- [15] L. Meitner, *Z. Physik* **17**, 54 (1923); P. Auger, *Compt. Rend T* **177**, 169 (1923).
- [16] T.A. Carlson, *Photoelectron and Auger Spectroscopy*, (Plenum Press, New York, 1975).
- [17] J. Berkowitz, *Photoabsorption, Photoionization, and Photoelectron Spectroscopy*, (Academic Press, New York, 1979).
- [18] W. Eberhardt, G. Kalkoffen, and C. Kunz, *Phys. Rev. Lett.* **41**, 156 (1978).
- [19] G.B. Armen, H. Aksela, T. Åberg, and S. Aksela, *J. Phys. B* **33**, R49 (2000).
- [20] J. Jauhiainen, H. Aksela, O.-P. Sairanen, E. Nömmiste, and S. Aksela, *J. Phys. B* **29**, 3385 (1996).
- [21] W. Mehlhorn, *Electron Spectrometry of Auger and Autoionizing States: Experiment and Theory*, (Universität Freiburg, Freiburg).
- [22] W. Mehlhorn, *Phys. Lett.* **26A**, 166 (1968).
- [23] U. Fano and D. Dill, *Phys. Rev. A* **6**, 185 (1972); J.W. Cooper, *Phys. Rev. A* **39**, 3714 (1989).
- [24] A. Starace, *Theory of Atomic Photoionization*, in *Handbuch der Physik* XXXI, Ed. W. Mehlhorn (Springer-Verlag, Berlin, 1982).
- [25] N.M. Kabachnik and I.P. Sazhina, *J. Phys. B* **17**, 1335 (1984); N.M. Kabachnik, B. Lohmann, and W. Mehlhorn, *J. Phys. B* **24**, 2249 (1991).
- [26] J. Tulkki, *Phys. Rev. Lett.* **62**, 2817 (1989).
- [27] V. Schmidt, *Rep. Prog. Phys.* **55**, 1483 (1992).
- [28] M. Meyer, A. Marquette, A.N. Grum-Grzhimailo, U. Kleiman, and B. Lohmann, *Phys. Rev. A* **64**, 022703 (2001).
- [29] H. Schmoranzer, S. Lauer, F. Vollweiler, A. Ehresmann, V.L. Sukhorukov, B.M. Lagutin, I.D. Petrov, Ph.V. Demekhin, K.-H. Schartner, B. Magel, and G. Mentzel, *J. Phys. B* **30**, 4463 (1997); A. Ehresmann, H. Schäffer, F. Vollweiler, G. Mentzel, B. Magel, K.-H. Schartner, and H. Schmoranzer, *J. Phys. B* **31**, 1487 (1998).
- [30] G. Margaritondo, *Introduction to Synchrotron Radiation*, (Oxford University Press, New York, 1988); G. Margaritondo, *Elements of Synchrotron Light*, (Oxford University Press, New York, 2002).

- [31] D. Attwood, *Soft X-Rays and Extreme Ultraviolet Radiation: Principles and Applications*, (Cambridge University Press, New York, 2000).
- [32] W.B. Peatman, *Gratings, Mirrors, and Slits: Beamline Design for Soft X-Ray Synchrotron Radiation Sources*, (Gordon and Breach Science Publishers, Amsterdam, 1997).
- [33] M. Bässler, A. Ausmees, M. Jurvansuu, R. Feifel, J.-O. Forsell, P. de Tarso Fonseca, A. Kivimäki, S. Sundin, S.L. Sorensen, R. Nyholm, O. Björneholm, S. Aksela, and S. Svensson, *Nucl. Instrum. Methods* **469**, 382 (2001).
- [34] H. Aksela, S. Aksela, and N.M. Kabachnik in *VUV and Soft X-Ray Photoionization*, Eds. U. Becker and D.A. Shirley, (Plenum Press, London, 1996).
- [35] M. Bässler, J.-O. Forsell, O. Björneholm, R. Feifer, M. Jurvansuu, S. Aksela, S. Sundin, S.L. Sorensen, R. Nyholm, A. Ausmees, and S. Svensson, *J. Electron Spectrosc. Relat. Phenom.* **101-103**, 953 (1999).
- [36] K.C. Prince, R.R. Blyth, R. Delaunay, M. Zitnik, J. Krempasky, J. Slezak, R. Camilloni, L. Avaldi, M. Coreno, G. Stefani, C. Furlani, M. de Simone, and S. Stranges, *J. Synchrotron Radiat.* **5**, 565 (1998); R.R. Blyth, R. Delaunay, M. Zitnik, J. Krempasky, R. Krempaska, J. Slezak, K.C. Prince, R. Richter, M. Vondracek, R. Camilloni, L. Avaldi, M. Coreno, G. Stefani, C. Furlani, M. de Simone, S. Stranges, M.-Y. Adam, *J. Electron Spectrosc. Relat. Phenom.* **101-103**, 959 (1999).
- [37] N. Mårtensson, P. Baltzer, P.A. Brühwiler, J.-O. Forsell, A. Nilsson, A. Stenborg, and B. Wannberg, *J. Electron Spectrosc. Relat. Phenom.* **70**, 117 (1994).
- [38] K.-H. Schartner, P. Lenz, B. Möbus, H. Schmoranzer, and M. Wildberger, *Phys. Lett. A* **128**, 374 (1988); H. Schmoranzer, H. Liebel, F. Vollweiler, R. Müller-Albrecht, A. Ehresmann, K.-H. Schartner, and B. Zimmermann, *Nucl. Instrum. Methods* **467-468**, 1526 (2001); G.C. King and K.-H. Schartner in *VUV and Soft X-Ray Photoionization*, Ed. U. Becker and D.A. Shirley, (Plenum Press, London, 1996).
- [39] K.-H. Schartner, P. Lenz, B. Möbus, B. Magel, H. Schmoranzer, and M. Wildberger, *Phys. Script.* **41**, 853 (1990).
- [40] M. Meyer, S. Aloise, and A.N. Grum-Grzhimailo, *Phys. Rev. Lett.* **88**, 223001 (2002); E. Melero García, A. Kivimäki, L.G.M. Petterson, J. Álvarez Ruiz, M. Coreno, M. de Simone, R. Richter, and K.C. Prince, *Phys. Rev. Lett.* **96**, 063003 (2006).

- [41] K.-H. Schartner, B. Möbus, P. Lenz, H. Schmoranzer, and M. Wildberger, *Phys. Rev. Lett.* **61**, 2744 (1988); K.-H. Schartner, P. Lenz, B. Möbus, H. Schmoranzer, and M. Wildberger, *J. Phys. B* **22**, 1573 (1989).
- [42] A.N. Grum-Grzhimailo, S. Fritzsche, P. O’Keeffe, and M. Meyer, *J. Phys. B* **38**, 2545 (2005); S. Kammer, K.-H. Schartner, S. Mickat, R. Schill, A. Ehresmann, L. Werner, S. Klumpp, H. Schmoranzer, I.D. Petrov, Ph.V. Demekhin, and V.L. Sukhorukov, *J. Phys. B.* **39**, 2757 (2006); V.L. Sukhorukov, I.D. Petrov, Ph.V. Demekhin, H. Schmoranzer, S. Mickat, S. Kammer, K.-H. Schartner, S. Klumpp, L. Werner, and A. Ehresmann, *J. Phys. B* **40**, 1295 (2007).
- [43] J. Jimenéz-Mier, C.D. Caldwell, M.G. Flemming, S.B. Whitfield, and P. van der Meulen, *Phys. Rev. A* **48**, 442 (1993).
- [44] P. Baltzer, L. Karlsson, M. Lundqvist, and B. Wannberg, *Rev. Sci. Instrum* **64**, 2179 (1993).
- [45] K. Ueda, M. Kitajima, A. De Fanis, Y. Tamemori, H. Yamaoka, H. Shindo, T. Furuta, T. Tanaka, H. Tanaka, H. Yoshida, R. Sankari, S. Aksela, S. Fritzsche, and N.M. Kabachnik, *Phys. Rev. Lett.* **90**, 153005 (2003).
- [46] G. Brown, M.H. Chen, B. Crasemann, and G.E. Ice, *Phys. Rev. Lett.* **45**, 1937 (1980).
- [47] T. Åberg and G. Howat in *Corpuscles and Radiation in Matter I*, Handbuch der Physik XXXI, Eds. S. Flügge and W. Mehlhorn, (Springer-Verlag, Berlin, 1982).
- [48] A. Kivimäki, A. Naves de Brito, S. Aksela, H. Aksela, O.-P. Sairanen, A. Ausmees, S.J. Osborne, L.B. Dantas, and S. Svensson, *Phys. Rev. Lett.* **71**, 4307 (1993).
- [49] G.C. King, M. Tronc, F.H. Read, and R.C. Bradford, *J. Phys. B* **10**, 2479 (1977).
- [50] T.X. Carroll, J.D. Bozek, E. Kukk, V. Myrseth, L.J. Sæthre, T.D. Thomas, and K. Wiesner, *J. Electron Spectrosc. Relat. Phenom.* **125**, 127 (2002).
- [51] J. Jauhiainen, A. Ausmees, A. Kivimäki, S.J. Osborne, A. Naves de Brito, S. Aksela, S. Svensson, and H. Aksela, *J. Electron Spectrosc. Relat. Phenom.* **69**, 181 (1994).
- [52] E.L. Kosarev, *Inverse Problems* **6**, 55 (1990); V.I. Gelfgat, E.L. Kosarev, and E.R. Podolyak, *Comput. Phys. Commun.* **74**, 335 (1993).

- [53] I.P. Grant, *Adv. Phys.* **19**, 747 (1970).
- [54] I.P. Grant, B.J. McKenzie, P.H. Norrington, D.F. Mayers, and N.C. Pyper, *Comp. Phys. Comm.* **21**, 207 (1980); K.G. Dyll, I.P. Grant, C.T. Johnson, F.A. Parpia, and E.P. Plummer, *Comp. Phys. Comm.* **55**, 425 (1989).
- [55] P.A.M. Dirac, *Proc. Roy. Soc. A* **117**, 610 (1928).
- [56] F.A. Parpia, C. Froese Fischer, and I.P. Grant, *Comp. Phys. Comm.* **94**, 249 (1996).
- [57] S. Fritzsche and I.P. Grant, *Comput. Phys. Comm.* **103**, 277 (1997); S. Fritzsche and J. Anton, *Comput. Phys. Comm.* **124**, 353 (2000).
- [58] T. Åberg, *Ann. Acad. Sci. Fenn. A VI* **308**, 1 (1969).
- [59] G. Wentzel, *Z. Phys.* **34**, 524 (1927).
- [60] S.M. Blinder, *Foundations of Quantum Dynamics*, (Academic Press, London, 1974).
- [61] M. Huttula, E. Kukk, S. Heinäsmäki, M. Jurvansuu, S. Fritzsche, H. Aksela, and S. Aksela, *Phys. Rev. A* **69**, 012702 (2004).
- [62] A. Mäntykenttä, H. Aksela, S. Aksela, J. Tulkki, and T. Åberg, *Phys. Rev. A* **47**, 4865 (1993).
- [63] S. Fritzsche, A. Surzhykov, and T. Stöhlker, *Phys. Rev. A* **72**, 012704 (2005).
- [64] S. Fritzsche, *J. Electron Spectrosc. Relat. Phenom.* **114-116**, 1155 (2001); S. Fritzsche, *Phys. Scr., T* **100**, 37 (2002).
- [65] S. Fritzsche and C. Froese Fischer, *Comput. Phys. Comm.* **99**, 323 (1997); S. Fritzsche, C. Froese Fischer, and C.Z. Dong, *Comput. Phys. Commun.* **124**, 340 (2000).
- [66] S. Fritzsche, B. Fricke, and W.-D. Sepp, *Phys. Rev. A* **45**, 1465 (1992).
- [67] U. Hergenhahn, N.M. Kabachnik, and B. Lohmann, *J. Phys. B* **24**, 4759 (1991).
- [68] S.B. Whitfield, J. Tulkki, and T. Åberg, *Phys. Rev. A* **44**, R6983 (1991).

- [69] H. Aksela, J. Jauhiainen, E. Kukkk, E. Nömmiste, S. Aksela, and J. Tulkki, *Phys. Rev. A* **53**, 290 (1996); H. Aksela, J. Jauhiainen, E. Nömmiste, S. Aksela, S. Sundin, A. Ausmees, and S. Svensson, *Phys. Rev. A* **54**, 605 (1996); M. Kitajima, M. Okamoto, Y. Shimizu, H. Chiba, S. Fritzsche, N.M. Kabachnik, I.P. Sazhina, F. Koike, T. Hayaishi, H. Tanaka, Y. Sato, and K. Ueda, *J. Phys. B* **34**, 3829 (2001).
- [70] E. Kukkk, H. Aksela, A. Kivimäki, J. Jauhiainen, E. Nömmiste, and S. Aksela, *Phys. Rev. A* **56**, 1481 (1997).
- [71] U. Fano, *Phys. Rev.* **124**, 1866 (1961), U. Fano and J.W. Cooper, *Phys. Rev.* **137**, A 1364 (1965).
- [72] D. Dill, *Phys. Rev. A* **7**, 1976 (1973).
- [73] N.M. Kabachnik and I.P. Sazhina, *J. Phys. B* **23**, L353 (1990); N.M. Kabachnik and A.N. Grum-Grzhimailo, *J. Phys. B* **34**, L63 (2001).
- [74] P. O’Keeffe, S. Aloïse, M. Meyer, and A.N. Grum-Grzhimailo, *Phys. Rev. Lett.* **90**, 023002 (2003); P. O’Keeffe, S. Aloïse, S. Fritzsche, B. Lohmann, U. Kleiman, M. Meyer, and A.N. Grum-Grzhimailo, *Phys. Rev. A* **70**, 012705 (2004).
- [75] S. Sorensen, T. Åberg, J. Tulkki, E. Rachlew-Källne, G. Sundström, and M. Kirm, *Phys. Rev. A* **50**, 1218 (1994).
- [76] B.M. Lagutin, I.D. Petrov, V.L. Sukhorukov, S. Kammer, S. Mickat, R. Schill, K.-H. Schartner, A. Ehresmann, Yu.A. Shutov, and H. Schmoranzler, *Phys. Rev. Lett.* **90**, 073001 (2003).
- [77] M. Martins, K. Godehusen, T. Richter, Ph. Wernet, and P. Zimmermann, *J. Phys. B* **39**, R79 (2006).
- [78] A. von dem Borne, R.L. Johnson, B. Sonntag, M. Talkenberg, A. Verweyen, Ph. Wernet, J. Schulz, K. Tiedtke, Ch. Gerth, B. Obst, P. Zimmermann, and J.E. Hansen, *Phys. Rev. A* **62**, 052703 (2000).
- [79] J. Väyrynen and S. Aksela, *J. Electron Spectrosc. Relat. Phenom.* **23**, 119 (1981).
- [80] Ch. Gerth, K. Godehusen, M. Richter, P. Zimmermann, J. Schulz, Ph. Wernet, B. Sonntag, A.G. Kochur, and I.D. Petrov, *Phys. Rev. A* **61**, 022713 (2000).
- [81] B.M. Lagutin, I.D. Petrov, Ph.V. Demekhin, V.L. Sukhorukov, F. Vollweiler, H. Liebel, A. Ehresmann, S. Lauer, H. Schmoranzler, O. Wilhelmi, B. Zimmermann, and K.-H. Schartner, *J. Phys. B* **33**, 1337 (2000).

- [82] B. Zimmermann, O. Wilhelmi, K.-H. Schartner, F. Vollweiler, H. Liebel, A. Ehresmann, S. Lauer, H. Schmoranzer, B.M. Lagutin, I.D. Petrov, and V.L. Sukhorukov, *J. Phys B* **33**, 2467 (2000); R.H. Schill, D. Hasselkamp, S. Kammer, S. Mickat, B. Zimmermann, K.-H. Schartner, A. Ehresmann, H. Schmoranzer, M. Schlüter, Yu.A. Schutov, B.M. Lagutin, and V.L. Sukhorukov, *J. Phys. B* **36**, L57 (2003).
- [83] J. Tulkki, H. Aksela, N.M. Kabachnik, *Phys. Rev. A* **50**, 2366 (1994); S.-M. Huttula, S. Alitalo, H. Aksela, S. Heinäsmäki, A. Kivimäki, J. Tulkki, M. Jurvansuu, E. Nömmiste, and S. Aksela, *Chem. Phys.* **289**, 81 (2003).
- [84] K.-H. Schartner, R.H. Schill, D. Hasselkamp, S. Mickat, S. Kammer, L. Werner, S. Klumpp, A. Ehresmann, H. Schmoranzer, B.M. Lagutin, and V.L. Sukhorukov, *J. Phys. B* **38**, 4155 (2005); K.-H. Schartner, R. Schill, D. Hasselkamp, S. Mickat, S. Kammer, L. Werner, S. Klumpp, A. Ehresmann, H. Schmoranzer, B.M. Lagutin, and V.L. Sukhorukov, *J. Phys. B* **40**, 1443 (2007); B.M. Lagutin, I.D. Petrov, V.L. Sukhorukov, Ph.V. Demekhin, B. Zimmermann, S. Mickat, S. Kammer, K.-H. Schartner, A. Ehresmann, Yu.A. Shutov, and H. Schmoranzer, *J. Phys. B* **36**, 3251 (2003).
- [85] S. Fritzsche, J. Nikkinen, S.-M. Huttula, H. Aksela, M. Huttula, and S. Aksela, *Phys. Rev. A* **75**, 012501 (2007).
- [86] A. Kivimäki, S. Heinäsmäki, M. Jurvansuu, S. Alitalo, E. Nömmiste, H. Aksela, and S. Aksela, *J. Electron Spectrosc. Relat. Phenom.* **114-116**, 49 (2001); Y. Shimizu, H. Yoshida, K. Okada, Y. Muramatsu, N. Saito, H. Ohashi, Y. Tamenori, S. Fritzsche, N.M. Kabachnik, H. Tanaka, and K. Ueda, *J. Phys. B* **33**, L685 (2000).
- [87] H. Ohashi, E. Ishiguro, Y. Tamenori, H. Okumura, A. Hiraya, H. Yoshida, Y. Senba, K. Okada, N. Saito, I.H. Suzuki, K. Ueda, T. Ibuki, S. Nagaoka, I. Koyano, and T. Ishikawa, *Nucl. Instr. Methods A* **467-468**, 533 (2001).